Commun. Comput. Phys.
doi: 10.4208/cicp.OA-2016-0173

Vol. **22**, No. 5, pp. 1224-1257
November 2017

A Second-Order Cell-Centered Lagrangian Method for Two-Dimensional Elastic-Plastic Flows

Jun-Bo Cheng[1], Yueling Jia[1,*], Song Jiang[1], Eleuterio F. Toro[2] and Ming Yu[1]

[1] *Laboratory of Computational Physics, Institute of Applied Physics and Computational Mathematics, Beijing, 100094, China.*
[2] *Laboratory of Applied Mathematics, University of Trento, Trento, Italy.*

Received 8 October 2016; Accepted (in revised version) 29 March 2017

Abstract. For 2D elastic-plastic flows with the hypo-elastic constitutive model and von Mises' yielding condition, the non-conservative character of the hypo-elastic constitutive model and the von Mises' yielding condition make the construction of the solution to the Riemann problem a challenging task. In this paper, we first analyze the wave structure of the Riemann problem and develop accordingly a **F**our-**R**arefaction wave approximate **R**iemann **S**olver with **E**lastic waves (**FRRSE**). In the construction of FRRSE one needs to use an iterative method. A direct iteration procedure for four variables is complex and computationally expensive. In order to simplify the solution procedure we develop an iteration based on two nested iterations upon two variables, and our iteration method is simple in implementation and efficient. Based on FRRSE as a building block, we propose a 2nd-order cell-centered Lagrangian numerical scheme. Numerical results with smooth solutions show that the scheme is of second-order accuracy. Moreover, a number of numerical experiments with shock and rarefaction waves demonstrate the scheme is essentially non-oscillatory and appears to be convergent. For shock waves the present scheme has comparable accuracy to that of the scheme developed by Maire et al., while it is more accurate in resolving rarefaction waves.

AMS subject classifications: 35L50, 35Q74, 74C05, 74F10, 74M20

Key words: Cell-centered Lagrangian scheme, high-order scheme, hypo-elastic constitutive model, four-rarefaction Riemann solver with elastic waves.

1 Introduction

This paper aims at the construction of a high-order cell-centered Lagrangian scheme for elastic-plastic flows in two-spatial dimensions with the isotropic elastic-plastic model,

*Corresponding author. *Email addresses:* jia_yueling@iapcm.ac.cn (Y. L. Jia), cheng_junbo@iapcm.ac.cn (J.-B. Cheng), jiang@iapcm.ac.cn (S. Jiang), eleuterio.toro@unitn.it (E. F. Toro), Yu_ming@iapcm.ac.cn (M. Yu)

 ©2017 Global-Science Press

https://doi.org/10.4208/cicp.OA-2016-0173 Published online by Cambridge University Press

initially developed by Wilkins [1]. The scheme is constructed based on an approximate Riemann solver for the equations of the elastic-plastic solids. In Wilkins' model, a perfectly elastic material is characterized by Hooke's law in terms of an incremental strain resulting in an incremental stress and Von Mises' yielding condition is used to describe the elastic limit. The earliest simulation for elastic-plastic hydrodynamic equations with Wilkins' model was developed by Wilkins in 1962 [1], in which the equations of momentum and specific internal energy are discretized on a staggered grid and artificial viscosity is employed to simulate moving shocks in order to damp spurious numerical oscillations. Besides the staggered Lagrangian approach, Eulerian and cell-centered Lagrangian schemes have also been used in the simulation of elastic-plastic flows.

Eulerian methods [8]- [12] are suitable for problems involving discontinuous waves and large deformations. However, most of them are for problems with the hyper-elastic model for isotropic materials. Compared with staggered Lagrangian schemes, cell-centered Lagrangian schemes have their own advantages. For the cell-centered Lagrangian scheme it is not necessary to use artificial viscosity and the scheme is conservative because the equation for total energy conservation, not the specific internal energy, is discretised. In recent years, the cell-centered Lagrangian scheme has attracted much attention [2]- [5], where cell-centered Lagrangian schemes are not only constructed for the hyper-elastic models, but also for hypo-elastic models. In these papers, a nodal Riemann solver is deduced from conservation of the total energy, but the structure of the Riemann solution is not fully exploited. Some authors, such as in [6] and [7], have utilized the structure of the solution of the Riemann problem to construct Riemann solvers for the governing equations with hypo-elastic models. Gavrilyuk et al. [7] analyzed the structure of the solution to the Riemann problem and developed a Riemann solver for the hyperbolic nonconservative model with a system of linear elasticity for transverse waves. Besides, the elastic energy is included in the total energy and an extra evolution equation is added in order to make the elastic transform reversible in the absence of shock waves. Després [6] constructed a shock solution to the non-conservative equations with the hypo-elasticity model and found that a sonic point was necessary to give a compression solution that begins at a constrained compressed state.

In this paper, we first analyze the structure of the solution of the Riemann problem for the governing equations with hypo-elastic models in the normal direction to a generic cell edge in two-spatial dimensions, then construct a four-rarefaction approximate Riemann solver with elastic waves (FRRSE) for the non-conservative equations of Wilkins' model with von Mises' yielding condition. Moreover, we use our FRRSE to define a numerical flux to construct a high-order cell-centered Lagrangian scheme.

The paper is organized as follows. We describe the governing equations in two-spatial dimensions in Section 2, our FRRSE is introduced in Section 3 and an associated high order cell-centered Lagrangian scheme for non-conservative elastic-plastic flows is developed in Section 4. A number of numerical examples are presented in Section 5 to validate our scheme, and conclusions follow in Section 6.

https://doi.org/10.4208/cicp.OA-2016-0173 Published online by Cambridge University Press

2 Governing equations in two-spatial dimensions

The equations of motion describing the dynamics of a two-dimensional homogeneous solid are

$$\partial_t \mathbf{U}+\partial_x \mathbf{F}(\mathbf{U})+\partial_y \mathbf{G}(\mathbf{U})=0, \quad x,y\in\Omega\subset\mathbb{R}^2, \quad t>0. \tag{2.1}$$

Here

$$\mathbf{U}=\begin{bmatrix}\rho\\ \rho u\\ \rho v\\ \rho E\end{bmatrix}, \quad \mathbf{F}=\begin{bmatrix}\rho u\\ \rho u^2-\sigma_x\\ \rho uv-s_{xy}\\ (\rho E-\sigma_x)u-s_{xy}v\end{bmatrix}, \quad \mathbf{G}=\begin{bmatrix}\rho v\\ \rho uv-s_{xy}\\ \rho v^2-\sigma_y\\ (\rho E-\sigma_y)v-s_{xy}u\end{bmatrix};$$

ρ is the density, u and v are the velocities in the x- and y-directions respectively, $E=e+\frac{1}{2}(u^2+v^2)$ with e being the specific internal energy denotes the total energy per unit mass, p is the hydrostatic pressure, $\sigma_x=-p+s_{xx}$ and $\sigma_y=-p+s_{yy}$ are the components of the Cauchy stress. s_{xx}, s_{yy} and s_{xy} are the deviatoric stresses.

In this paper we consider the Mie-Grüneisen equation of state:

$$p(\rho,e)=\rho_0 a_0^2 f(\eta)+\rho_0\Gamma_0 e, \quad f(\eta)=\frac{(\eta-1)\left[\eta-\frac{1}{2}\Gamma_0(\eta-1)\right]}{\left[\eta-s(\eta-1)\right]^2}, \quad \eta=\frac{\rho}{\rho_0}.$$

The incremental constitutive law is given by

$$\frac{d\mathbf{S}}{dt}=2\mu\mathbf{D}_0-(\mathbf{SW}-\mathbf{WS}), \quad \mathbf{S}=\begin{bmatrix}s_{xx} & s_{xy}\\ s_{xy} & s_{yy}\end{bmatrix}, \tag{2.2}$$

where μ is the shear modulus, $\mathbf{S}$ is the deviatoric stress, $\mathbf{D}_0=\mathbf{D}-\frac{1}{3}\mathbf{tr}(\mathbf{D})\mathbf{I}_d$, $\mathbf{D}$ is the strain rate tensor and

$$\mathbf{D}=\frac{1}{2}\left[\nabla\mathbf{v}+(\nabla\mathbf{v})^T\right], \qquad \mathbf{W}=\frac{1}{2}\left[\nabla\mathbf{v}-(\nabla\mathbf{v})^T\right], \mathbf{v}=(u,v)^T.$$

The von Mises' yielding condition is used to describe the elastic limit. In two-dimensional spaces, it is given by $\mathbf{S}=\mathbf{S}\times\min\left(1,Y_0/\sqrt{\frac{3}{2}(\mathbf{S}:\mathbf{S})}\right)$, where Y_0 is the yielding strength of the material in simple tension.

3 FRRSE: approximate Riemann solver

We consider the Riemann problem of the elastic-plastic equations in the y-direction:

https://doi.org/10.4208/cicp.OA-2016-0173 Published online by Cambridge University Press

$$\left.\begin{aligned}
&\partial_t \mathbf{U}+\partial_y \mathbf{G}(\mathbf{U})=0,\\
&\partial_t s_{xx}+v\partial_y s_{xx}+\tfrac{2}{3}\mu\partial_y v-s_{xy}\partial_y u=0,\\
&\partial_t s_{yy}+v\partial_y s_{yy}-\tfrac{4}{3}\mu\partial_y v+s_{xy}\partial_y u=0,\\
&\partial_t s_{xy}+v\partial_y s_{xy}-\left(\mu+\tfrac{s_{yy}-s_{xx}}{2}\right)\partial_y u=0,\\
&\mathbf{S}=\mathbf{S}\times\min\left(1,\frac{Y_0}{\sqrt{\frac{3}{2}(\mathbf{S}:\mathbf{S})}}\right),\ \mathbf{Q}=[\rho,\rho u,\rho v,\rho E,s_{xx},s_{yy},s_{xy}]^T,\\
&\mathbf{Q}(x,y,t=0)=\begin{cases}\mathbf{Q}_L & \text{if } x<0,\\ \mathbf{Q}_R & \text{if } x\geq 0.\end{cases}
\end{aligned}\right\} \tag{3.1}$$

The genuinely nonlinear waves in the solution of the Riemann problem (3.1) are either shock or rarefaction waves. Our aim is to build four-rarefaction approximate Riemann solver with elastic waves (FRRSE). A Riemann solver based on the assumption that all four genuinely nonlinear waves are rarefaction waves is in fact exact when four genuinely nonlinear waves are actually rarefaction waves. Otherwise it is an approximate solver, that is when one or more genuinely nonlinear waves are shock waves. Just like a two-rarefaction Riemann solver (TRRS) in conventional gas dynamics [18], FRRSE is very robust.

3.1 Analysis of the Jacobian matrix

For the Mie-Grüneisen EOS, (3.1) can be written in terms of the primitive variables as

$$\partial_t \mathbf{W}+\mathbf{B}(\mathbf{W})\partial_y \mathbf{W}=0, \tag{3.2}$$

where $\mathbf{W}=(\rho,u,v,p,s_{xx},s_{yy},s_{xy})^T$, with $\Gamma=\frac{\rho_0\Gamma_0}{\rho}$, $\mathbf{B}(\mathbf{W})$ is given by

$$\mathbf{B}(\mathbf{W})=\begin{bmatrix}
v & 0 & \rho & 0 & 0 & 0 & 0\\
0 & v & 0 & 0 & 0 & 0 & -\frac{1}{\rho}\\
0 & 0 & v & \frac{1}{\rho} & 0 & -\frac{1}{\rho} & 0\\
0 & -\Gamma s_{xy} & \rho a^2-\Gamma s_{yy} & v & 0 & 0 & 0\\
0 & -s_{xy} & \frac{2}{3}\mu & 0 & v & 0 & 0\\
0 & s_{xy} & -\frac{4}{3}\mu & 0 & 0 & v & 0\\
0 & -\mu-\frac{s_{yy}-s_{xx}}{2} & 0 & 0 & 0 & 0 & v
\end{bmatrix}, \tag{3.3}$$

$$a^2=\frac{\partial p}{\partial \rho}+\frac{p}{\rho^2}\frac{\partial p}{\partial e}=a_0^2\frac{\partial f}{\partial \eta}+\frac{p}{\rho^2}\rho_0\Gamma_0. \tag{3.4}$$

The eigenvalues of (3.3) are given by

$$\lambda_1=\lambda_2=\lambda_3=v,\quad \lambda_4=v-s_1,\quad \lambda_5=v+s_1,\quad \lambda_6=v-s_2,\quad \lambda_7=v+s_2, \tag{3.5}$$

https://doi.org/10.4208/cicp.OA-2016-0173 Published online by Cambridge University Press

where

$$s_1=\sqrt{\frac{1}{\rho}\left(\mu+\frac{s_{yy}-s_{xx}}{2}\right)},\quad s_2=\sqrt{a^2-\frac{\rho_0}{\rho^2}\Gamma_0 s_{yy}+\frac{4}{3}\frac{\mu}{\rho}}. \tag{3.6}$$

From the above equations, we can see that if

$$\mu>\left|\frac{s_{yy}-s_{xx}}{2}\right|\quad\text{and}\quad\frac{4}{3}\mu>\left|\frac{\rho_0}{\rho}\Gamma_0 s_{yy}\right|, \tag{3.7}$$

the system (3.2) is hyperbolic. For real materials, because the shear modulus μ is much greater than Y^0, the use of von Mises' yielding condition makes μ much greater than s_{xx} and s_{yy}, which means (3.7) is always satisfied for real materials.

The corresponding right eigenvectors are given by

$$\begin{aligned}
&r_1=(0,0,0,1,0,1,0)^T,\quad r_2=(0,0,0,0,1,0,0)^T,\quad r_3=(1,0,0,0,0,0,0)^T, \\
&r_4=\left(w_1w_2,\frac{1}{\rho s_1},-w_0w_2,w_1\left(w_3-\frac{4\mu}{3\rho}w_2\right),w_1\left(1+\frac{2\mu}{3\rho}w_2\right),-w_1\left(1+\frac{4\mu}{3\rho}w_2\right),1\right)^T, \\
&r_5=\left(w_1w_2,-\frac{1}{\rho s_1},w_0w_2,w_1\left(w_3-\frac{4\mu}{3\rho}w_2\right),w_1\left(1+\frac{2\mu}{3\rho}w_2\right),-w_1\left(1+\frac{4\mu}{3\rho}w_2\right),1\right)^T, \\
&r_6=\left(\frac{-3\rho}{4\mu},0,\frac{3s_2}{4\mu},1-\frac{3\rho s_2^2}{4\mu},-\frac{1}{2},1,0\right)^T,\quad r_7=\left(\frac{-3\rho}{4\mu},0,\frac{-3s_2}{4\mu},1-\frac{3\rho s_2^2}{4\mu},-\frac{1}{2},1,0\right)^T,
\end{aligned} \tag{3.8}$$

where

$$w_0=\frac{s_{xy}}{\rho^2 s_1},\quad w_1=\frac{s_{xy}}{\rho s_1^2},\quad w_2=\frac{1+\Gamma}{s_1^2-s_2^2},\quad w_3=\frac{s_2^2+s_1^2\Gamma}{s_1^2-s_2^2}. \tag{3.9}$$

3.2 Wave structure of the Riemann problem

Theoretically, based on the assumption that all non-linear waves are rarefaction, according to the different characteristic velocities of the left and right torsional and longitudinal stress waves, there are four kinds of structures in the solution to the Riemann problem (3.2) in the x-t plane. It consists of 7 waves emanating from the origin, one for each eigenvalue λ_i in (3.5): $\lambda_1=\lambda_2=\lambda_3=v$ mean three linearly degenerate waves with same characteristic velocity, thus we regards them as ONE in the structure waves; λ_4 and λ_5 are two **T**orsional **S**tress **W**aves (**TSW**s), while λ_6 and λ_7 are two **L**ongitudinal **S**tress **W**aves (**LSW**s).

While for real materials, since the shear modulus μ is much greater than Y^0, i.e., μ is much greater than s_{xx} and s_{yy}, this means that s_1 is always less than s_2. Therefore, $v_L-s_{2L}<v_L-s_{1L}<v_R+s_{1R}<v_R+s_{2R}$, which is shown in Fig. 1.

Besides the above case in Fig. 1, there are other possible cases: if both states ahead of and behind a shear wave are all in the plastic field, then the shear wave does not exist. In other words, the state ahead of the shear wave is NOT equal to that behind the shear wave. So, there are other possible three cases in the full waves structure of the Riemann problem here. We shall show how to deal with these cases in the following.

https://doi.org/10.4208/cicp.OA-2016-0173 Published online by Cambridge University Press

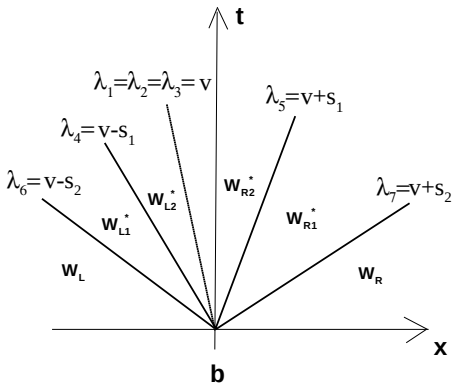


Figure 1: Possible wave patterns in the solution of the Riemann problem.

Linearly degenerate waves

Using the eigenvectors (3.8) of the primitive variable formulation, for the λ_1 wave we have

$$\frac{d\rho}{0}=\frac{du}{0}=\frac{dv}{0}=\frac{dp}{1}=\frac{ds_{xx}}{0}=\frac{ds_{yy}}{1}=\frac{ds_{xy}}{0}, \tag{3.10}$$

which means that

$$\rho^*_{L2}=\rho^*_{R2},\quad u^*_{L2}=u^*_{R2},\quad v^*_{L2}=v^*_{R2},\quad s^*_{xx,L2}=s^*_{xx,R2},\quad s^*_{xy,L2}=s^*_{xy,R2}, \tag{3.11}$$

where $()^*_{Lk}$ and $()^*_{Rk}(k=1,2)$ mean $()$ in the region of $\mathbf{W}^*_{Lk}$ and $\mathbf{W}^*_{Rk}(k=1,2)$ respectively.

Besides, from (3.10) we can see that

$$\frac{d(s_{yy})}{1}=\frac{dp}{1}=\frac{d(s_{yy}-p)}{1-1}=\frac{d\sigma_y}{0},$$

which means that

$$\sigma^*_{y,L2}=\sigma^*_{y,R2}. \tag{3.12}$$

Using the same method, for the λ_2 wave we have

$$\frac{d\rho}{0}=\frac{du}{0}=\frac{dv}{0}=\frac{dp}{0}=\frac{ds_{xx}}{1}=\frac{ds_{yy}}{0}=\frac{ds_{xy}}{0},$$

then we can get

$$\rho^*_{L2}=\rho^*_{R2},\quad u^*_{L2}=u^*_{R2},\quad v^*_{L2}=v^*_{R2},\quad p^*_{L2}=p^*_{R2},\quad s^*_{yy,L2}=s^*_{yy,R2},\quad s^*_{xy,L2}=s^*_{xy,R2}. \tag{3.13}$$

Combining the forth and fifth equations in (3.14) yields

$$\sigma^*_{y,L2}=\sigma^*_{y,R2}. \tag{3.14}$$

https://doi.org/10.4208/cicp.OA-2016-0173 Published online by Cambridge University Press

In the same way, for the λ_3 wave we have

$$\frac{d\rho}{1}=\frac{du}{0}=\frac{dv}{0}=\frac{dp}{0}=\frac{ds_{xx}}{0}=\frac{ds_{yy}}{0}=\frac{ds_{xy}}{0},$$

which means that

$$u^*_{L2}=u^*_{R2},\quad v^*_{L2}=v^*_{R2},\quad p^*_{L2}=p^*_{R2},\quad s^*_{xx,L2}=s^*_{xx,R2},\quad s^*_{yy,L2}=s^*_{yy,R2},\quad s^*_{xy,L2}=s^*_{xy,R2}. \tag{3.15}$$

From the above third and fifth equations, we can see

$$\sigma^*_{y,L2}=\sigma^*_{y,R2}. \tag{3.16}$$

From the eigenvector analysis above, for all the linearly degenerate waves (λ_1, λ_2 and λ_3), it holds that

$$u^*_{L2}=u^*_{R2},\quad v^*_{L2}=v^*_{R2},\quad \sigma^*_{y,L2}=\sigma^*_{y,R2},\quad s^*_{xy,L2}=s^*_{xy,R2}. \tag{3.17}$$

Here we do not show the details of analysis for the simplicity of presentation.

TSWs which are along $\frac{dy}{dt}=v\pm s_1$

Across two TSWs associated with $\lambda_{4,5}=v\mp s_1$, one has

$$d\rho=\frac{1+\Gamma}{(s_1^2-s_2^2)\rho s_1^2}d\Big(\frac{s_{xy}^2}{2}\Big),\quad dp=\frac{(w_3-\frac{4\mu}{3\rho}w_2)}{\rho s_1^2}d\Big(\frac{s_{xy}^2}{2}\Big), \tag{3.18}$$

$$ds_{xx}=\frac{(1+\frac{2\mu}{3\rho}w_2)}{\rho s_1^2}d\Big(\frac{s_{xy}^2}{2}\Big),\quad ds_{yy}=\frac{-(1+\frac{4\mu}{3\rho}w_2)}{\rho s_1^2}d\Big(\frac{s_{xy}^2}{2}\Big), \tag{3.19}$$

$$dv=\frac{\mp w_2}{\rho^2 s_1}d\Big(\frac{s_{xy}^2}{2}\Big),\quad du=\frac{\pm ds_{xy}}{\rho s_1}. \tag{3.20}$$

LSWs which are along $\frac{dy}{dt}=v\pm s_2$

Across two LSWs associated with $\lambda_{6,7}=v\mp s_2$, one has

$$\begin{cases} du=ds_{xy}=0,\quad dv\pm\frac{s_2}{\rho}d\rho=0,\\ dp+\Big(\frac{4\mu}{3\rho}-s_2^2\Big)d\rho=0,\quad ds_{xx}=\frac{2\mu}{3\rho}d\rho,\quad ds_{yy}=\frac{-4\mu d\rho}{3\rho}. \end{cases} \tag{3.21}$$

We use the subscript 'a' or 'b' to denote the state ahead of or behind a wave. In order to evaluate the states in the central star regions clearly and legibly, the procedure of evaluating the states behind the LSWs and TSWs are introduced in Appendixes A, B and C.

https://doi.org/10.4208/cicp.OA-2016-0173 Published online by Cambridge University Press

3.3 Equations in the central star regions

The central star regions states around the linearly degenerate wave are called $\mathbf{W}^*_{L2}$ and $\mathbf{W}^*_{R2}$ depicted in Fig. 1. From (A.1) and (C.1)-(C.4), we know there are four unknown variables: $s^{T*}_{xy,L}$, $s^{T*}_{xy,R}$, ρ^{L*}_L, ρ^{L*}_R, where the subscripts L and R denote the left and right states, the superscripts $T*$ and $L*$ denote the states behind a TSW and a LSW, respectively.

Basic analysis: Just like the case of a fluid, the normal velocity v and the normal stress σ_y are always continuous across the linearly degenerate wave, while the tangential velocity u and the tangential stress s_{xy} may not be continuous **when the stress(stresses) is (are) in the plastic regime**. If one of two states behind two TSWs is in the plastic regime, s_{xy} is no longer continuous across the linearly degenerate wave, but the tangential velocity u may be continuous and we need to solve the following half Riemann problem $u^{T*}_{L/R}(s^{T*}_{xy,L/R}) = u^E_{R/L}$. After obtaining the solution, von Mises' yielding condition is used. If the evaluated state is in the plastic regime, one needs to evaluate the state of elastic limit. The detailed evaluation method is given in Appendix B.

According to the above analysis, there are four cases needed to be considered.

Case 1: If any state behind every wave is not in the plastic regime, then according to (3.17), one can get the following four equations:

$$\begin{cases} (u^*_{L2},v^*_{L2},\sigma^*_{y,L2})^T(\rho^{L*}_L,s^{T*}_{xy,L}) = (u^*_{R2},v^*_{R2},\sigma^*_{y,R2})^T(\rho^{L*}_R,s^{T*}_{xy,R}), \\ s^{T*}_{xy,L} = s^{T*}_{xy,R}. \end{cases} \tag{3.22}$$

Case 2: Assume the stress behind the left TSW is in the plastic regime, while that behind the right TSW is not, then one can get the following relations:

$$\begin{cases} (v^*_{L2},\sigma^*_{y,L2})^T(\rho^{L*}_L,s^{T*}_{xy,L}) = (v^*_{R2},\sigma^*_{y,R2})^T(\rho^{L*}_R,s^{T*}_{xy,R}), \\ u^*_{L2} = u^E_{L2}, \quad s^{T*}_{xy,L} = s^E_{xy,L2}, \quad u^*_{R2}(\rho^{L*}_R,s^{T*}_{xy,R}) = u^E_{L2}, \end{cases} \tag{3.23}$$

where the superscript E means the elastic limit. At last, the above equations can be simplified as

$$\begin{cases} (v^*_{L2},\sigma^*_{y,L2})^T(\rho^{L*}_L,s^E_{xy,L2}) = (v^*_{R2},\sigma^*_{y,R2})^T(\rho^{L*}_R,s^{T*}_{xy,R}), \\ u^*_{L2} = u^E_{L2}, \quad s^{T*}_{xy,L} = s^E_{xy,L2}, \quad u^*_{R2}(\rho^{L*}_R,s^{T*}_{xy,R}) = u^E_{L2}. \end{cases} \tag{3.24}$$

Case 3: Assume the stress behind the right TSW is in the plastic regime, while that behind the left TSW is not, then using the same method as that in Case 2, one can get the following relations:

$$\begin{cases} (v^*_{L2},\sigma^*_{y,L2})^T(\rho^{L*}_L,s^{T*}_{xy,L}) = (v^*_{R2},\sigma^*_{y,R2})^T(\rho^{L*}_R,s^E_{xy,R2}), \\ u^*_{R2} = u^E_{R2}, \quad s^{T*}_{xy,R} = s^E_{xy,R2}, \quad u^*_{L2}(\rho^{L*}_L,s^{T*}_{xy,L}) = u^E_{R2}, \end{cases} \tag{3.25}$$

Case 4: Assume both stresses behind two TSWs are all in the plastic regime, one can get the following relations:

$$\begin{cases} (v^*_{L2},\sigma^*_{y,L2})^T(\rho^{L*}_L,s^E_{xy,L2}) = (v^*_{R2},\sigma^*_{y,R2})^T(\rho^{L*}_R,s^E_{xy,R2}), \\ u^*_{L2} = u^E_{L2},\ u^*_{R2} = u^E_{R2},\ s^{T*}_{xy,R} = s^E_{xy,R2},\ s^{T*}_{xy,L} = s^E_{xy,L2}. \end{cases} \tag{3.26}$$

https://doi.org/10.4208/cicp.OA-2016-0173 Published online by Cambridge University Press

3.4 Main ideas of solving the main equations

First solve (3.22) and obtain its solutions without considering elastic limit. If any state behind two TSWs is not in the plastic regime, then the evaluation is stopped. If two states are in the plastic regime, we have to evaluate elastic limits of two states. If only one state is in the plastic regime, we need to compute the half Riemann problem, and then use von Mises' yielding condition.

Two nested iterations: There are four variables and four equations, this means the above equations are solvable. On the other hand, it is difficult to directly solve (3.22) because the above equations are strongly nonlinear. Hence, it is necessary to use an iteration method to solve it. But the iteration of four variables is difficult and expensive. Instead, we use here two small nested iterations of two variables to replace the above iteration of four variables. Obviously, comparing with the iteration of four variables, our two nested iterations of two variables are simple and computationally cheap.

The two nested iterations include an outer iteration and an inner iteration. The **outer iteration** is to solve the following equations:

$$v^*_{L2}(\rho^{L*}_{xy,L})=v^*_{R2}(\rho^{L*}_{xy,R}),\quad \sigma^*_{y,L2}(\rho^{L*}_{xy,L})=\sigma^*_{y,R2}(\rho^{L*}_{xy,R}). \tag{3.27}$$

The **inner iteration** is to solve the equations in the tangential direction of a cell interface. These equations have four cases:

$$\begin{cases} \textbf{Case a}: & u^*_{L2}(s^{T*}_{xy,L})=u^*_{R2}(s^{T*}_{xy,R}), & s^{T*}_{xy,L}=s^{T*}_{xy,R};\\ \textbf{Case b}: & u^*_{L2}(s^{T*}_{xy,L})=u^E_{R2}, & s^{T*}_{xy,R}=s^E_{xy,R2};\\ \textbf{Case c}: & u^*_{R2}(s^{T*}_{xy,R})=u^E_{L2}, & s^{T*}_{xy,L}=s^E_{xy,L2};\\ \textbf{Case d}: & u^*_{L2}=u^E_{L2},\ u^*_{R2}=u^E_{R2}, & s^{T*}_{xy,L}=s^E_{xy,L2},\ s^{T*}_{xy,R}=s^E_{xy,R2}. \end{cases} \tag{3.28}$$

The problem (3.28) is called the problem of two TSWs. The detailed procedure of solving this problem is introduced in Appendix D.

The main procedure of two nested iterations is summarized below.

Main procedure:

Define $G(\rho^{L*}_L,\rho^{L*}_R)=-(p^*_{R2}-p^*_{L2})+s^*_{yy,R2}-s^*_{yy,L2}$ and $F(\rho^{L*}_L,\rho^{L*}_R)=v^*_{R2}-v^*_{L2}$. By virtue of $v^*_{L2}=v^*_{R2}$ and $\sigma^*_{y,L2}=\sigma^*_{y,R2}$,

$$F(\rho^{L*}_L,\rho^{L*}_R)=0,\quad G(\rho^{L*}_L,\rho^{L*}_R)=0. \tag{3.29}$$

We shall use the Newton iteration method to solve (3.29) as follows.

Step 1: Guess $\rho^{L*}_{L,(k)}$ and $\rho^{L*}_{R,(k)}$ behind the left and right LSWs, where k means the k-th iteration. For $k=1$, we take $\rho^{L*}_{L,(1)}=\rho^{L*}_{R,(1)}=\frac{\rho_L+\rho_R}{2}$.

Step 2: Evaluate $\mathbf{W}^{L*}_{L1,(k)}$ and $\mathbf{W}^{L*}_{R1,(k)}$.

https://doi.org/10.4208/cicp.OA-2016-0173 Published online by Cambridge University Press

Step 3: Solve (3.28) with the known initial states ahead of two TSWs to give $\mathbf{W}^{T*}_{L2,(k)}$ and $\mathbf{W}^{T*}_{R2,(k)}$. The detailed procedure is shown in Appendix D.

Step 4: Evaluate $F_{(k)}=v_{R2,(k)}-v_{L2,(k)}$ and $G_{(k)}=(s_{yy,R2,(k)}-p_{R2,(k)})-(s_{yy,L2,(k)}-p_{L2,(k)})$;

Step 5: Evaluate the derivatives of $F_{(k)}(G_{(k)})$ with respect to $\rho^{L*}_{L,(k)}(\rho^{L*}_{R,(k)})$;

Step 6: Evaluate the values of $\rho^{L*}_{L,(k+1)}$ and $\rho^{L*}_{R,(k+1)}$

$$\begin{bmatrix} \rho^{L*}_{R,(k+1)} \\ \rho^{L*}_{L,(k+1)} \end{bmatrix} = \begin{bmatrix} \rho^{L*}_{R,(k)} \\ \rho^{L*}_{L,(k)} \end{bmatrix} - \begin{bmatrix} F_{(k)} \\ G_{(k)} \end{bmatrix} \begin{bmatrix} \frac{\partial F_{(k)}}{\partial \rho^{L*}_R} & \frac{\partial F_{(k)}}{\partial \rho^{L*}_L} \\ \frac{\partial G_{(k)}}{\partial \rho^{L*}_R} & \frac{\partial G_{(k)}}{\partial \rho^{L*}_L} \end{bmatrix}^{-1}. \tag{3.30}$$

Step 7: Evaluate the errors of the iteration:

$$\mathrm{CHA}=\max\left[\frac{\left|\rho^{L*}_{L,(k+1)}-\rho^{L*}_{L,(k)}\right|}{\frac{1}{2}\left|\rho^{L*}_{L,(k+1)}+\rho^{*}_{L,(k)}\right|},\frac{\left|\rho^{L*}_{R,(k+1)}-\rho^{L*}_{R,(k)})\right|}{\frac{1}{2}\left|\rho^{L*}_{R,(k+1)}+\rho^{L*}_{R,(k)}\right|},|F_{(k)}|,|G_{(k)}|\right].$$

If $\mathrm{CHA}<10^{-6}$, then stop the iteraton. Otherwise, go to Step 2 with $K:=K+1$.

In the following, we give the derivatives of $F_{(k)}$ and $G_{(k)}$ with respect to $\rho^{L*}_{L,(k)}$ and $\rho^{L*}_{R,(k)}$.

$$\begin{cases} \frac{\partial F_{(k)}}{\partial \rho^{L*}_{L,(k)}}=\frac{s_2\left(\rho^{L*}_{L,(k)}\right)}{\rho^{*}_{L,(k)}}-\frac{\triangle v_{tL}}{\triangle \rho_{tL}}, \quad \frac{\partial F_{(k)}}{\partial \rho^{L*}_{R,(k)}}=\frac{s_2\left(\rho^{L*}_{R,(k)}\right)}{\rho^{*}_{R,(k)}}+\frac{\triangle v_{tR}}{\triangle \rho_{tR}}, \\ \frac{\partial G_{(k)}}{\partial \rho^{L*}_{L,(k)}}=s_2^2\left(\rho^{L*}_{L,(k)}\right)-\frac{\triangle s_{yy,L,(k)}}{\triangle \rho_{L,(k)}}+\frac{\triangle P_{tL}-\triangle s_{yy,tL}}{\triangle \rho_{tL}}-\frac{4\mu}{3\rho^{*}_{L,(k)}}, \\ \frac{\partial G_{(k)}}{\partial \rho^{L*}_{R,(k)}}=-s_2^2\left(\rho^{L*}_{R,(k)}\right)+\frac{\triangle s_{yy,R,(k)}}{\triangle \rho_{R,(k)}}-\frac{\triangle P_{tR}-\triangle s_{yy,tR}}{\triangle \rho_{tR}}+\frac{4\mu}{3\rho^{*}_{R,(k)}}, \end{cases}$$

where $\triangle \iota_{tm}=\iota^{T*}_{m,(k)}-\iota^{L*}_{m,(k)}$, $\iota=\rho,v,p,s_{yy}$ and $m=L,R$. We compute the derivative of s_{yy} in the density by the finite difference method. In the numerical tests below we find that this method is very efficient.

In the above iteration, Step 3 is an inner iteration, the iteration of evaluating ρ^{L*}_L and ρ^{L*}_R is an outer iteration.

4 A second-order cell-centered Lagrangian scheme

We consider an initial boundary value problem for (2.1). For a Lagrangian scheme, the governing equations also include the equations of moving coordinates at vertices of grids:

$$\frac{dx(t)}{dt}=u(x,y,t), \quad \frac{dy(t)}{dt}=v(x,y,t). \tag{4.1}$$

In this paper we use the second-order predictor-corrector method to discretize all the equations.

https://doi.org/10.4208/cicp.OA-2016-0173 Published online by Cambridge University Press

4.1 Predictor step

4.1.1 Second-order reconstruction method

In this paper, we use a simple WENO reconstruction approach to perform the reconstruction procedure. Define

$$\mathbf{W}=\left(\rho,u,v,p,s_{xx},s_{yy},s_{xy}\right)^T. \tag{4.2}$$

Given the spatial averages of $\mathbf{W}(x,y)$ in $N\times M$ cells:

$$\overline{W}_{i,j}=\frac{1}{V_{i,j}}\int_{I_{i,j}}\mathbf{W}(x,y)dxdy, \qquad i=1,\cdots,N, \quad j=1,\cdots,M, \tag{4.3}$$

where N and M are the numbers of cells in x- and y-directions respectively, $I_{i,j}$ denotes the cell C_0. We reconstruct the point-wise values of $\mathbf{W}$ at the mid point of four cell edges and require the reconstructed values to be of second-order accuracy.

We apply the second-order WENO reconstruction approach to approximate the value of $\mathbf{W}$ at the mid point of four cell edges, with the approximation essentially non-oscillatory (ENO).

In our second-order WENO reconstruction, eight stencils are used (eight cells around C_0, see Fig. 4). Let us denote these eight stencils by s_k, $k=1,\cdots,8$, where

$$s_k=\{C_0,C_k,C_{k+1}\}, \tag{4.4}$$

where cells C_0-C_8 can be found in Fig. 2.

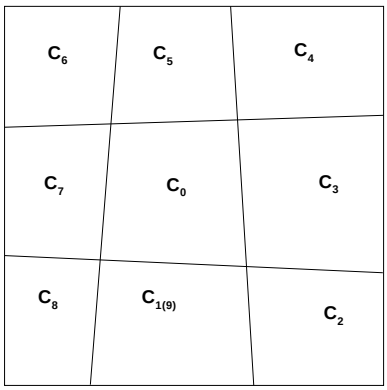


Figure 2: Cell C_0 with ambient 8 cells (c_1-c_8) for reconstruction.

From the value of $\mathbf{W}$ at each stencil s_k, we can construct a second-order approximation polynomial

$$\mathbf{p}_k(x,y)=\mathbf{W}_{0,k}+\mathbf{W}_{1,k}x+\mathbf{W}_{2,k}y. \tag{4.5}$$

https://doi.org/10.4208/cicp.OA-2016-0173 Published online by Cambridge University Press

At last, the second-order WENO polynomial for cell (i,j) is given by

$$\mathbf{p}_{i,j}(x,y)=\sum_{k=1}^{8}\omega_k\mathbf{p}_k(x,y), \tag{4.6}$$

where ω_k $(k=1,\cdots,8)$ are the WENO weights of $\mathbf{W}$ at the kth stencil,

$$\omega_k=\frac{1}{(\varepsilon^2+\mathbf{W}_{1,k}^2+\mathbf{W}_{2,k}^2)}\Big/\sum_{l=1}^{8}\frac{1}{\left(\varepsilon^2+\mathbf{W}_{1,l}^2+\mathbf{W}_{2,l}^2\right)},\quad \varepsilon=10^{-6}. \tag{4.7}$$

The point-wise values of $\mathbf{W}$ at the mid point of four edges of cell C_0 are given by

$$\begin{cases}\mathbf{W}_{i,j,D}=\mathbf{p}_{i,j}(x_i,y_{j-\frac{1}{2}}), & \mathbf{W}_{i,j,U}=\mathbf{p}_{i,j}(x_i,y_{j+\frac{1}{2}}),\\ \mathbf{W}_{i,j,L}=\mathbf{p}_{i,j}(x_{i-\frac{1}{2}},y_j), & \mathbf{W}_{i,j,R}=\mathbf{p}_{i,j}(x_{i+\frac{1}{2}},y_j).\end{cases} \tag{4.8}$$

4.1.2 Evaluation of the Godunov values

We solve the classical homogeneous Riemann problem for time dependent elastic-plastic equations in the y-direction:

$$\left.\begin{aligned}&\text{PDEs:}\begin{cases}\partial_t\mathbf{U}+\partial_y\mathbf{G}(\mathbf{U})=0,\\ \partial_t s_{xx}+v\partial_y s_{xx}+\frac{2}{3}\mu\partial_y v-s_{xy}\partial_y u=0,\\ \partial_t s_{yy}+v\partial_y s_{yy}-\frac{4}{3}\mu\partial_y v+s_{xy}\partial_y u=0,\\ \partial_t s_{xy}+v\partial_y s_{xy}-\left(\mu+\frac{s_{yy}-s_{xx}}{2}\right)\partial_y u=0,\end{cases}\\ &\text{ICs: }\mathbf{Q}(x_{i+\frac{1}{2}},y,0)=\begin{cases}\mathbf{Q}_{i,j,U} & \text{if}\quad y<y_j^n,\\ \mathbf{Q}_{i,j+1,D} & \text{if}\quad y>y_j^n.\end{cases}\end{aligned}\right\} \tag{4.9}$$

$\mathbf{Q}_{i,j,U}$ and $\mathbf{Q}_{i,j+1,D}$ are functions of $\mathbf{W}_{i,j,U}^n$ and $\mathbf{W}_{i,j+1,D}^n$ given by Eq. (4.8).

Denote the solution of (4.9) by $\mathbf{D}^{(0)}(y/t)$, then the Godunov values of $\mathbf{Q}$ are $\mathbf{Q}_{i,j+\frac{1}{2}}^n=\mathbf{D}^{(0)}(v)$. Because the grid moves at speed of the flow, the Godunov values of $\mathbf{Q}$ should be the values of $\mathbf{Q}$ at the linearly degenerate waves of the Riemann solution. Here we use the upwind method to define the Godunov values at the linearly degenerate waves.

Step A1: Evaluate W_{L2}^* and W_{R2}^* in Fig. 1.

Step A2: Determine $(\rho^*,u^*,v^*,p^*,s_{xx}^*,s_{yy}^*,s_{xy}^*)$ of $(\rho,u,v,p,s_{xx},s_{yy},s_{xy})$:

$$\left(\rho^*,u^*,v^*,p^*,s_{xx}^*,s_{yy}^*,s_{xy}^*\right)=\begin{cases}W_{L2}^* & \text{if}\quad \frac{v_{L2}^*+v_{R2}^*}{2}>0,\\ W_{R2}^* & \text{if}\quad \frac{v_{L2}^*+v_{R2}^*}{2}\le 0.\end{cases} \tag{4.10}$$

Given $(\rho^*,u^*,v^*,p^*,s_{xx}^*,s_{yy}^*,s_{xy}^*)$, we can compute the Godunov values of $\mathbf{Q}$.

https://doi.org/10.4208/cicp.OA-2016-0173 Published online by Cambridge University Press

4.1.3 Evaluation of the vertex velocity

Fig. 3 depicts a node P shared by four edges (1,2,3,4) and four cells $\{C_1, C_2, C_3$ and $C_4\}$. P_k is the mid point of edge k, the length and the unit outward normal of the edge $[P,P_k]$ are denoted by L_k and $\overrightarrow{n}_k$ respectively. The normal velocity at P_k is $v_{n,k}$, which is determined by solving the Riemann problem introduced in Section 4.1.2.

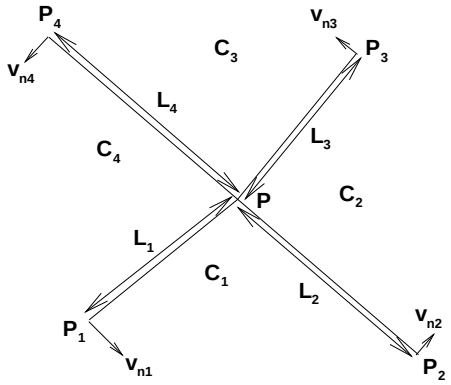


Figure 3: Node P with 4 edges and 4 cells (C_1,C_2,C_3 and C_4) surrounded.

The momentum is conservative around a node: $\sum_{k=1}^{4}\left[m_k\left(\overrightarrow{v}_p\cdot\overrightarrow{n_k}-v_{n,k}\right)\cdot\overrightarrow{n_k}\right]=0$, where $m_k=\frac{1}{2}(\rho_{c_{k-1}}s_{2,k-1}+\rho_{c_k}s_{2,k})L_k$. Finally, the resulting equations can be written as

$$\mathbf{M}_P\cdot\overrightarrow{v}_P=\mathbf{F}_{PC}=\begin{pmatrix}\sum_{k=1}^{4}m_k n_{x,k}v_{n,k}\\ \sum_{k=1}^{4}m_k n_{y,k}v_{n,k}\end{pmatrix}, \tag{4.11}$$

where

$$\mathbf{M}_P=\begin{pmatrix}\sum_{k=1}^{4}m_k n_{x,k}^2 & \sum_{k=1}^{4}m_k n_{x,k}n_{y,k}\\ \sum_{k=1}^{4}m_k n_{x,k}n_{y,k} & \sum_{k=1}^{4}m_k n_{y,k}^2\end{pmatrix}. \tag{4.12}$$

Solving the algebraic system (4.11), one gets the velocity $\overrightarrow{v}_p$ of node p.

4.1.4 Discretization of the moving equations

A two-dimensional spatial domain Ω is divided into $N\times M$ cells, $I_{i,j}$ denotes a quadrilateral cell constructed on $\overrightarrow{r}=(x,y)$ in proper order by 4 vertices subscripts $(i-\frac{1}{2},j-\frac{1}{2})$, $(i+\frac{1}{2},j-\frac{1}{2})$, $(i+\frac{1}{2},j+\frac{1}{2})$, $(i-\frac{1}{2},j+\frac{1}{2})$.

An integration of (4.1) from t^n to $t^{n+\frac{1}{2}}$ yields

$$\int_{t^n}^{t^{n+\frac{1}{2}}}\frac{d(x,y)_{i+\frac{1}{2},j+\frac{1}{2}}(t)}{dt}=\int_{t^n}^{t^{n+\frac{1}{2}}}(u,v)(x_{i+\frac{1}{2}},y_{j+\frac{1}{2}},t)dt. \tag{4.13}$$

https://doi.org/10.4208/cicp.OA-2016-0173 Published online by Cambridge University Press

In the predictor step, we perform obtain the coordinates of the grid vertex:

$$x^{n+\frac{1}{2}}_{i+\frac{1}{2},j+\frac{1}{2}}=x^{n}_{i+\frac{1}{2},j+\frac{1}{2}}+u^{n}_{i+\frac{1}{2},j+\frac{1}{2}}\frac{\Delta t}{2},\quad y^{n+\frac{1}{2}}_{i+\frac{1}{2},j+\frac{1}{2}}=y^{n}_{i+\frac{1}{2},j+\frac{1}{2}}+v^{n}_{i+\frac{1}{2},j+\frac{1}{2}}\frac{\Delta t}{2}.$$

4.1.5 Discretization of the conservative equations

The finite volume version of the second-order scheme follows from integrating (2.1) over $\Omega_{1234-abcd}$, denoted by Ω in Fig. 4, and has the following formulation by virtue of the Green's theorem:

$$\begin{aligned}S^{n+\frac{1}{2}}_{i,j}\overline{U}^{n+\frac{1}{2}}_{i,j}=&S^{n}_{i,j}\overline{U}^{n}_{i,j}-(\mathbf{F}_{i+\frac{1}{2},j}-\mathbf{F}_{i-\frac{1}{2},j}+\mathbf{F}_{i,j+\frac{1}{2}}-\mathbf{F}_{i,j-\frac{1}{2}})\\&+(\mathbf{G}_{i+\frac{1}{2},j}-\mathbf{G}_{i-\frac{1}{2},j}+\mathbf{G}_{i,j+\frac{1}{2}}-\mathbf{G}_{i,j-\frac{1}{2}}),\end{aligned}$$

where $S^{n+\frac{1}{2}}_{i,j}$ ($S^{n}_{i,j}$) denote the areas of $I_{i,j}$ at half (old) time, $\overline{\mathbf{U}}^{n}_{i,j}$ ($\overline{\mathbf{U}}^{n+\frac{1}{2}}_{i,j}$) is the cell spatial average at old (half) time. $\mathbf{F}_{i+\frac{1}{2},j}$ and $\mathbf{G}_{i,j+\frac{1}{2}}$ are given by

$$\left.\begin{aligned}\mathbf{F}_{i+\frac{1}{2},j}=&\int_{t^n}^{t^{n+\frac{1}{2}}}\int_{y_{i+\frac{1}{2},j-\frac{1}{2}}}^{y_{i+\frac{1}{2},j+\frac{1}{2}}}\mathbf{f}(\mathbf{U}(x_{i+\frac{1}{2},j},y,t))dydt=\frac{\Delta t\Delta y^{n}_{i+\frac{1}{2},j}}{2}\mathbf{f}(\mathbf{U}^{\mathbf{n}}_{\mathbf{i+\frac{1}{2},j}}),\\\mathbf{G}_{i,j+\frac{1}{2}}=&\int_{t^n}^{t^{n+\frac{1}{2}}}\int_{x_{i-\frac{1}{2},j+\frac{1}{2}}}^{x_{i+\frac{1}{2},j+\frac{1}{2}}}\mathbf{g}(\mathbf{U}(x,y_{i,j+\frac{1}{2}},t))dxdt=\frac{\Delta t\Delta x^{n}_{i,j+\frac{1}{2}}}{2}\mathbf{g}(\mathbf{U}^{\mathbf{n}}_{\mathbf{i,j+\frac{1}{2}}})\end{aligned}\right\}$$

with

$$\begin{aligned}\mathbf{f}=&\big(0,\,p-s_{xx},\,-s_{xy},\,(p-s_{xx})u-s_{xy}v\big)^T,\\\mathbf{g}=&\big(0,\,-s_{xy},\,p-s_{yy},\,(p-s_{yy})v-s_{xy}u\big)^T,\end{aligned}$$

and $\mathbf{U}^{\mathbf{n}}_{\mathbf{i+\frac{1}{2},j}}$ ($\mathbf{U}^{\mathbf{n}}_{\mathbf{i,j+\frac{1}{2}}}$) is the Godunov value of $\mathbf{U}$ at the cell interface $\overrightarrow{r}^{n}_{i+\frac{1}{2},j}$ ($\overrightarrow{r}^{n}_{i,j+\frac{1}{2}}$), and $\Delta y^{n}_{i+\frac{1}{2},j}=y^{n}_{i+\frac{1}{2},j+\frac{1}{2}}-y^{n}_{i+\frac{1}{2},j-\frac{1}{2}}$, $\Delta x^{n}_{i,j+\frac{1}{2}}=x^{n}_{i+\frac{1}{2},j+\frac{1}{2}}-x^{n}_{i-\frac{1}{2},j+\frac{1}{2}}$.

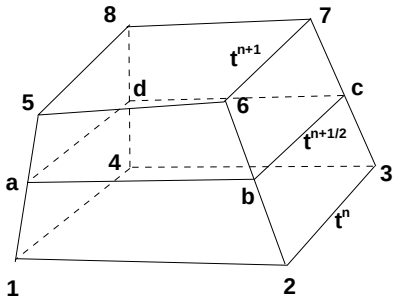


Figure 4: Integration volume.

https://doi.org/10.4208/cicp.OA-2016-0173 Published online by Cambridge University Press

4.1.6 Discretization of the constitutive equation

In this subsection, we discretize the constitutive equation (2.2). In the Lagrangian frame, it can be written as

$$\begin{cases} \frac{ds_{xx}}{dt}=2\mu(\frac{2}{3}\frac{\partial u}{\partial x}-\frac{1}{3}\frac{\partial v}{\partial y})+s_{xy}\left(\frac{\partial u}{\partial y}-\frac{\partial v}{\partial x}\right), \\ \frac{ds_{yy}}{dt}=2\mu(\frac{2}{3}\frac{\partial v}{\partial y}-\frac{1}{3}\frac{\partial u}{\partial x})-s_{xy}\left(\frac{\partial u}{\partial y}-\frac{\partial v}{\partial x}\right), \\ \frac{ds_{xy}}{dt}=\mu\left(\frac{\partial v}{\partial x}+\frac{\partial u}{\partial y}\right)+\frac{s_{yy}-s_{xx}}{2}\left(\frac{\partial u}{\partial y}-\frac{\partial v}{\partial x}\right). \end{cases} \tag{4.14}$$

The geometrical conservation law, which is very important for a cell-centered Lagrangian scheme, means that the following equation should be satisfied:

$$\frac{dV_{i,j}(t)}{dt}=\int\int_{I_{i,j}}\left(\frac{\partial u}{\partial x}+\frac{\partial v}{\partial y}\right)dxdy. \tag{4.15}$$

In two spatial dimensions, the volume of cell $I_{i,j}$ is defined as

$$\begin{aligned} V_{i,j}(t)=\frac{1}{2}\big[&(y_3-y_1)(x_2-x_1)-(x_3-x_1)(y_2-y_1) \\ &+(y_4-y_1)(x_3-x_1)-(x_4-x_1)(y_3-y_1)\big], \end{aligned}$$

where $(x_k,y_k)=(x_k(t),y_k(t))$, $k=1,2,3,4$, are the coordinates of the vertices of cell $I_{i,j}$. If we take the material derivative to the volume $V_{i,j}(t)$ of cell $I_{i,j}$, we obtain

$$\frac{dV_{i,j}(t)}{dt}=\sum_{k=1}^{4}\frac{u_k+u_{k+1}}{2}(y_{k+1}-y_k)-\frac{v_k+v_{k+1}}{2}(x_{k+1}-x_k), \tag{4.16}$$

where $(\cdot)_5=(\cdot)_1$, (u_k,v_k) is the moving velocity of the k-th vertex of cell $I_{i,j}$.

The geometrical conservative law is guaranteed by (4.16) and (4.15),

$$\int\int_{I_{i,j}}\left(\frac{\partial u}{\partial x}+\frac{\partial v}{\partial y}\right)dxdy=\sum_{k=1}^{4}\frac{u_k+u_{k+1}}{2}(y_{k+1}-y_k)-\frac{v_k+v_{k+1}}{2}(x_{k+1}-x_k).$$

We discretize $\int\int_{I_{i,j}}\frac{\partial u}{\partial x}dxdy$, $\int\int_{I_{i,j}}\frac{\partial v}{\partial y}dxdy$, $\int\int_{I_{i,j}}\frac{\partial u}{\partial y}dxdy$ and $\int\int_{I_{i,j}}\frac{\partial v}{\partial x}dxdy$ by

$$\left.\begin{aligned} (\bar{u_x},\bar{v}_x)&=\frac{1}{V_{i,j}^n}\int\int_{I_{i,j}}\frac{\partial(u,v)}{\partial x}dxdy=\frac{1}{V_{i,j}^n}\sum_{k=1}^{4}\frac{(u,v)_k+(u,v)_{k+1}}{2}(y_{k+1}-y_k), \\ (\bar{u_y},\bar{v}_y)&=\frac{1}{V_{i,j}^n}\int\int_{I_{i,j}}\frac{\partial(u,v)}{\partial y}dxdy=-\frac{1}{V_{i,j}^n}\sum_{k=1}^{4}\frac{(u,v)_k+(u,v)_{k+1}}{2}(x_{k+1}-x_k), \end{aligned}\right\}$$

https://doi.org/10.4208/cicp.OA-2016-0173 Published online by Cambridge University Press

Thanks to the above three equations, the system (4.14) is discretized as follows:

$$\left.\begin{aligned}
&\frac{\left(\bar{s}_{xx}\right)^{n+1/2}-\left(\bar{s}_{xx}\right)^{n}}{\frac{1}{2}\Delta t}=2\mu\left(\bar{u}_x-\frac{1}{3}\left(\bar{u}_x+\bar{v}_y\right)\right)+\bar{s}^n_{xy}\left(\bar{u}_y-\bar{v}_x\right),\\
&\frac{\left(\bar{s}_{yy}\right)^{n+1/2}-\left(\bar{s}_{yy}\right)^{n}}{\frac{1}{2}\Delta t}=2\mu\left(\bar{v}_y-\frac{1}{3}\left(\bar{u}_x+\bar{v}_y\right)\right)-\bar{s}^n_{xy}\left(\bar{u}_y-\bar{v}_x\right),\\
&\frac{\left(\bar{s}_{xy}\right)^{n+1/2}-\left(\bar{s}_{xy}\right)^{n}}{\frac{1}{2}\Delta t}=\mu\left(\bar{u}_y+\bar{v}_x\right)+\frac{\left(\bar{s}^n_{yy}-\bar{s}^n_{xx}\right)}{2}\left(\bar{u}_y-\bar{v}_x\right).
\end{aligned}\right\}$$

4.2 Corrector step

Using the predictor step, we obtain the cell average $\overline{\mathbf{Q}}^{n+\frac{1}{2}}$ of $\mathbf{Q}^{n+\frac{1}{2}}$. We perform the reconstruction procedure and compute the Godunov values of $\mathbf{Q}$ at half time, then we evaluate the moving speed of a grid node. All the equations are integrated over the control volume $\Omega_{1234-5678}$ and the form of the resulting equations is the same as that in the predictor step, while all the variables with the superscripts n on the right hand side of all the equations in the predictor step are replaced by the corresponding variables with the superscripts $n+\frac{1}{2}$.

5 Numerical tests

In this section, we test our scheme with several problems to validate the scheme in capturing the elastic-plastic waves and the convergence.

5.1 Accuracy test

We use smooth manufactured solutions to test the accuracy of our second-order scheme [15, 16]. We consider the following equations of compressible elastic-plastic flows with source terms:

$$\left.\begin{aligned}
&\partial_t\mathbf{U}+\partial_x\mathbf{F}(\mathbf{U})+\partial_y\mathbf{G}(\mathbf{U})=\mathcal{S},\\
&\tfrac{d\mathbf{S}}{dt}=2\mu\mathbf{D}_0-(\mathbf{SW}-\mathbf{WS}),
\end{aligned}\right\}$$

where $\mathcal{S}=(0,s_2,s_3,s_4)^T$, and

$$\begin{aligned}
s_2=&-2\rho_0\rho_x\pi x_1a^2+2b\rho_0\rho_y\pi y_1a+\rho_0(2a\rho_x\pi x_1-2b\rho_y\pi y_1)a,+2\pi s_1y_2\\
&+2\pi s_1x_2+2\pi s_1y_1+\frac{a_0^2\rho_0(\rho_x\Gamma_0\pi x_1-2\rho_x\pi x_1)z_1}{(-\rho_yy_2-\rho_xx_2-sz_1+1)^2}-\frac{2a_0^2\rho_0\rho_x\pi x_1\left(z_1-\frac{1}{2}\Gamma_0z_1+1\right)}{(-\rho_yy_2-\rho_xx_2-sz_1+1)^2}\\
&-\frac{2a_0^2\rho_0(2\rho_x\pi sx_1-2\rho_x\pi x_1)z_1\left(-\rho_yy_2-\rho_xx_2-\frac{1}{2}\Gamma_0z_1+1\right)}{(z_1-sz_1+1)^3},
\end{aligned}$$

https://doi.org/10.4208/cicp.OA-2016-0173 Published online by Cambridge University Press

$$
\begin{aligned}
s_3=&\frac{2\rho_0\rho_y\pi\left(z_1-\frac{1}{2}\Gamma_0 z_1+1\right)y_1a_0^2}{(z_1-sz_1+1)^2}+\frac{\rho_0 z_1(2\rho_y\pi y_1-\rho_y\Gamma_0\pi y_1)a_0^2}{(z_1-sz_1+1)^2}\\
&-\frac{2\rho_0 z_1\left(z_1-\frac{1}{2}\Gamma_0 z_1+1\right)(2\rho_y\pi y_1-2\rho_y\pi s y_1)a_0^2}{(z_1-sz_1+1)^3}+2\pi s_1x_1-2ab\rho_0\rho_x\pi x_1\\
&+2\pi s_1x_2+2\pi s_1y_1+2b^2\rho_0\rho_y\pi y_1+b\rho_0(2a\rho_x\pi x_1-2b\rho_y\pi y_1),\\
s_4=&-b(-2\pi s_1x_1-2\pi s_1x_2)+a\left(s_{421}+s_{422}-2\rho_0\rho_x\left(\frac{a^2}{2}+\frac{b^2}{2}+e_0\right)\pi x_1\right)\\
&+2a\pi s_1x_2+\rho_0\left(\frac{a^2}{2}+\frac{b^2}{2}+e_0\right)(2a\rho_x\pi x_1-2b\rho_y\pi y_1)-a(-2\pi s_1y_2-2\pi s_1y_1)\\
&+b\left(s_{441}+s_{442}+2\pi s_1y_1+2\rho_0\rho_y\left(\frac{a^2}{2}+\frac{b^2}{2}+e_0\right)\pi y_1\right),
\end{aligned}
$$

with

$$
\begin{aligned}
s_{421}=&\frac{\rho_0(\rho_x\Gamma_0\pi x_1-2\rho_x\pi x_1)z_1a_0^2}{(z_1-s(-\rho_y y_2-\rho_x x_2)+1)^2}-\frac{2\rho_0\rho_x\pi x_1\left(z_1-\frac{1}{2}\Gamma_0 z_1+1\right)a_0^2}{(z_1-sz_1+1)^2},\\
s_{422}=&-\frac{2\rho_0(2\rho_x\pi s x_1-2\rho_x\pi x_1)z_1\left(z_1-\frac{1}{2}\Gamma_0 z_1+1\right)a_0^2}{(z_1-s(z_1)+1)^3},\\
s_{441}=&\frac{2\rho_0\rho_y\pi\left(z_1-\frac{1}{2}\Gamma_0 z_1+1\right)y_1a_0^2}{(z_1-sz_1+1)^2}+\frac{\rho_0 z_1(2\rho_y\pi y_1-\rho_y\Gamma_0\pi y_1)a_0^2}{(z_1-sz_1+1)^2},\\
s_{442}=&-\frac{2\rho_0 z_1\left(z_1-\frac{1}{2}\Gamma_0 z_1+1\right)(2\rho_y\pi y_1-2\rho_y\pi s y_1)a_0^2}{(z_1-sz_1+1)^3}.
\end{aligned}
$$

In the above expressions, $a=b=10000\ m/s$, $\rho_x=\rho_y=0.1$, $s_1=60\times10^6\ Pa$, $e_0=10^{-14}$, $x_1=\cos(2\pi(x-at))$, $x_2=\sin(2\pi(x-at))$, $y_1=\sin(2\pi(y-bt))$, $y_2=\cos(2\pi(y-bt))$, $z_1=-\rho_y y_2-\rho_x x_2$, $\rho_0=8930\ kg/m^3$, $a_0=3940\ m/s$, $\Gamma_0=2$,$s=1.49$, the shear module $\mu=45\times10^9\ Pa$, the yielding strength $Y^0=90\times10^9\ Pa$.

The smooth manufactured solution of the above equations reads as

$$
\begin{aligned}
&\rho=\rho_0\left\{1-\rho_x\sin[2\pi(x-at)]-\rho_y\cos[2\pi(y-bt)]\right\},\\
&u=a,\quad v=b,\quad e=e_0,\quad s_{xx}=s_1(\cos(2\pi(x-at))-\sin(2\pi(y-bt))),\\
&s_{yy}=-s_1(\sin(2\pi(x-at))-\cos(2\pi(y-bt))),\quad s_{xy}=s_{xx}+s_{yy},
\end{aligned}
$$

where e_0 is the constant internal energy.

The computational domain is $[0,1]\times[0,1]$ and the periodic boundary condition is used. The initial data are

$$
\begin{aligned}
&\rho=\rho_0\left\{1-\rho_x\sin(2\pi x)-\rho_y\cos(2\pi y)\right\},\\
&u=a,\quad v=b,\quad e=e_0,\quad s_{xx}=s_1(\cos(2\pi x)-\sin(2\pi y)),\\
&s_{yy}=-s_1(\sin(2\pi x)-\cos(2\pi y)),\quad s_{xy}=s_{xx}+s_{yy}.
\end{aligned}
$$

https://doi.org/10.4208/cicp.OA-2016-0173 Published online by Cambridge University Press

We use our second-order Lagrangian scheme to simulate this problem. Because there are source terms in this problem, we apply the fifth-order Gaussian quadrature method to compute $\int\int_{I_{i,j}} s_2 dxdy$, $\int\int_{I_{i,j}} s_3 dxdy$ and $\int\int_{I_{i,j}} s_4 dxdy$, and here we omit the details of treating the source terms for the simplicity of presentation.

The errors in L_1- and L_∞-norms at the output time $t=1$ are given in Tables 1 and 2, from which we see that our scheme achieves the desired order of accuracy.

Table 1: Error in L_1-norm of our scheme for the smooth solution using $N\times N$ uniform mesh cells.

N	ρ	Ord	$\rho u+\rho v$	Ord	ρE	Ord	s_{xx}	Ord
20	6.87E-04		1.87E-03		1.09E-03		7.47E-05	
40	2.21E-04	1.64	4.86E-04	1.95	2.57E-04	2.09	2.47E-05	1.60
80	6.18E-05	1.84	1.27E-04	1.93	6.48E-05	1.99	6.86E-06	1.85
160	1.62E-05	1.93	3.28E-05	1.96	1.64E-05	1.98	1.79E-06	1.94

Table 2: Error in L_∞-norm of our scheme for the smooth solution using $N\times N$ uniform mesh cells.

N	ρ	Ord	$\rho u+\rho v$	Ord	ρE	Ord	s_{xx}	Ord
20	2.55E-03		8.13E-03		5.52E-03		3.07E-04	
40	8.01E-04	1.67	2.33E-03	1.80	1.50E-03	1.88	8.77E-05	1.81
80	2.24E-04	1.84	6.28E-04	1.89	3.97E-04	1.92	2.28E-05	1.95
160	5.73E-05	1.97	1.59E-04	1.98	1.00E-04	1.99	5.88E-06	1.95

5.2 A piston problem with stress shock waves in copper

Here we simulate a moving shock in a piece of copper with the same initial condition as that in [4]. The left boundary condition is a velocity boundary condition given by $v_{piston}=20\ m/s$, whereas on the right, upper and down boundaries of the computational domain, the wall boundary conditions are imposed.

In order to test the convergence of the current scheme, we compute this problem, to which there is the exact solution, with 100×8, 200×8, 400×8 and 800×8 cells, respectively. The CFL number is taken to be 0.45 and the stopping time is $t=150\ \mu s$. The numerical results with different Δx are presented in Fig. 5, from which we see that the numerical solution is converging to the exact solution, and the leading elastic shock wave and the followed plastic shock wave are well captured. Besides, there is no numerical oscillation near the shock waves. This asserts that the current scheme is right and stability.

Moreover, we compare the numerical results by our first-order and second-order schemes with those by the first-order and second-order schemes developed by Maire et al. [4] in Fig. 6, from which it is clear to see that there are very small differences in the results of both first-order schemes.

This shows that for shock waves, our Riemann solver works as well as the node Riemann solver in [4] from results by the first scheme. Besides, we can find that **our second-**

https://doi.org/10.4208/cicp.OA-2016-0173 Published online by Cambridge University Press

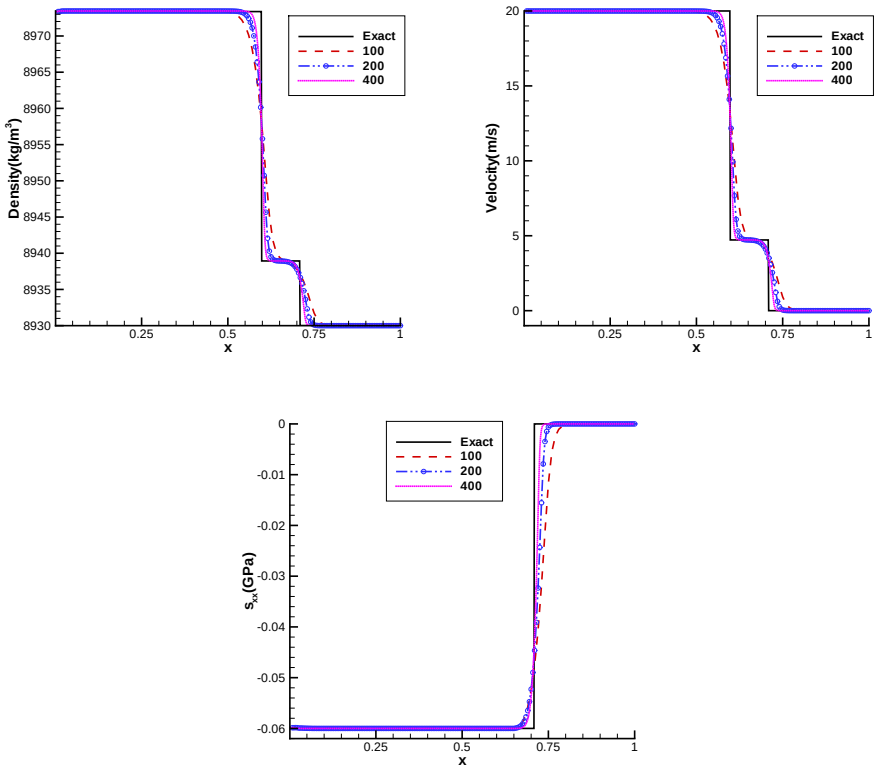


Figure 5: Piston problem. Density, velocity and s_{xx} versus x at time $t=150\ \mu s$.

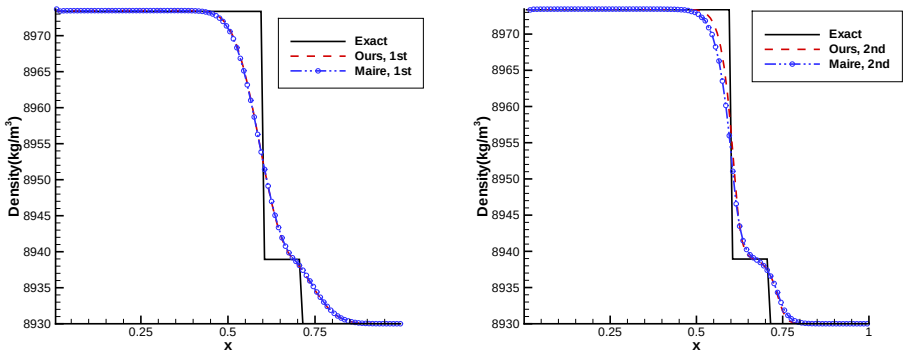


Figure 6: Piston problem. Comparison of the densities computed by the current 1st- and 2nd-order schemes and that by the 1st- and 2nd-order schemes developed by Maire et al. with 100 cells.

order scheme performs better for the shock waves than Maire et al.'s second-order scheme. It shows that our simple WENO reconstruction has higher accuracy(and smaller dissapitation shown in the test: two-dimensional projectile impact) than the piecewise linear reconstruction based on a least square approach introduced in [4].

https://doi.org/10.4208/cicp.OA-2016-0173 Published online by Cambridge University Press

5.3 Wilkins' problem

This problem is initially introduced by Wilkins in [1]. We test it here to show the ability of our scheme in the simulation of rarefaction waves. This problem describes a moving aluminium plate striking another aluminium plate. The equation of state for aluminium and the initial condition are the same as those in [4]. We use 400×8 and 800×8 cells to simulate the problem up to time 5×10^{-6} s with free boundary condition on the left boundary and wall boundary condition on the other three boundaries. Numerical results are presented in Figs. 7-9. The reference solution (solid line in all the figures) is obtained by using the current second-order cell-centered Lagrangian scheme with 4000×8 cells.

From Figs. 7-9 we observe that the numerical solution is converging to the reference one. Similarly, the elastic and plastic right-facing shocks and the reflected elastic and plastic rarefaction waves are well captured, and the numerical results are in good agreement with those in [4].

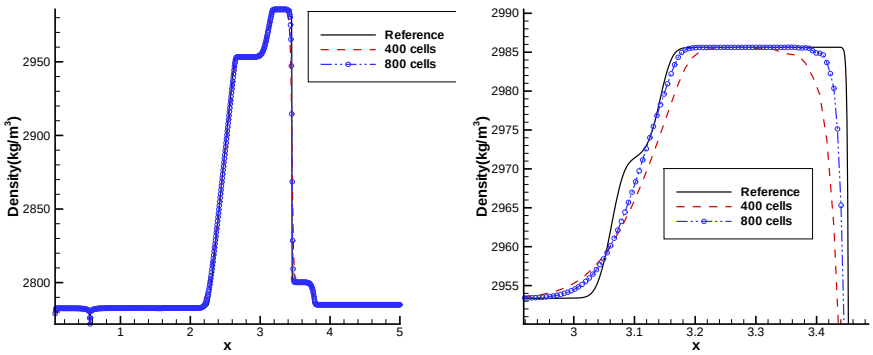


Figure 7: Wilkins' problem. Density versus x at time $t=5$ μs. Bottom figure: Close-up of the region around the head of the right-facing elastic rarefaction wave.

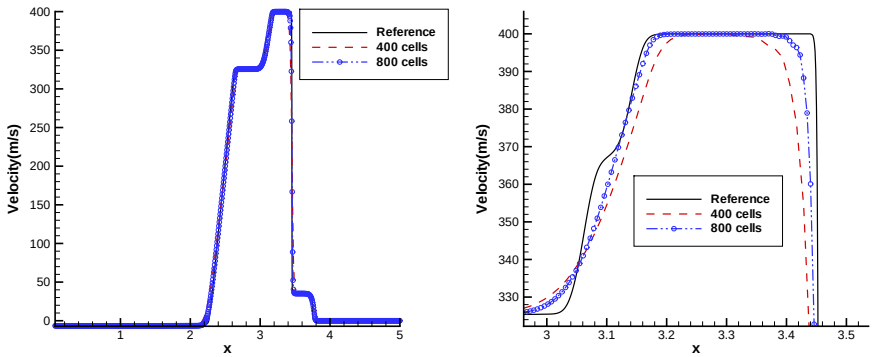


Figure 8: Wilkins' problem. Velocity versus x at time $t=5$ μs. Right figure: Close-up of the region around the head of the right-facing elastic rarefaction wave.

https://doi.org/10.4208/cicp.OA-2016-0173 Published online by Cambridge University Press

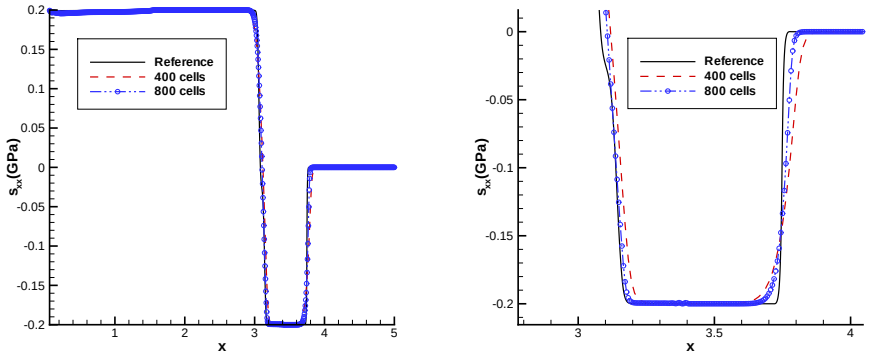


Figure 9: Wilkins' problem. s_{xx} versus x at time $t=5$ μs. Bottom figure: Close-up of the region around the head of the right-facing elastic shock wave.

We also compare the computed results by the current first-order and second-order schemes with those by the first-order and second-order schemes developed by Maire et al. in [4] in Figs. 10 and 11, from which it can be observed that

(1) The current first-order and second-order schemes perform better than Maire et al.'s first-order and second-order schemes around the plastic rarefaction wave. This is an advantage of FRRSE in resolving rarefaction waves.

(2) The numerical results computed by the current first-order scheme agree very well with those by Maire et al.'s first-order scheme around the elastic and plastic right-facing shocks. However, the current second-order scheme performs better than Maire et al.'s second-order scheme around the shocks. This demonstrates that the current reconstruction method has higher accuracy than the piecewise linear reconstruction method introduced in [4].

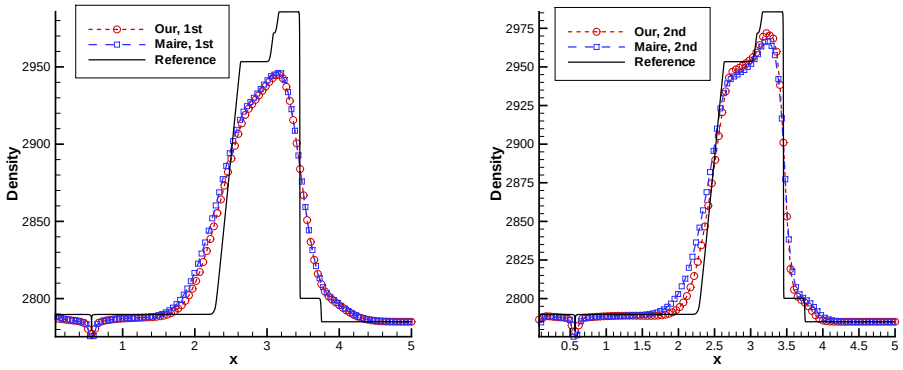


Figure 10: Wilkins' problem. Comparison between the computed densities by the current 1st-order and 2nd-order schemes and those by Maire et al.'s 1st-order and 2nd-order schemes with 100 cells.

https://doi.org/10.4208/cicp.OA-2016-0173 Published online by Cambridge University Press

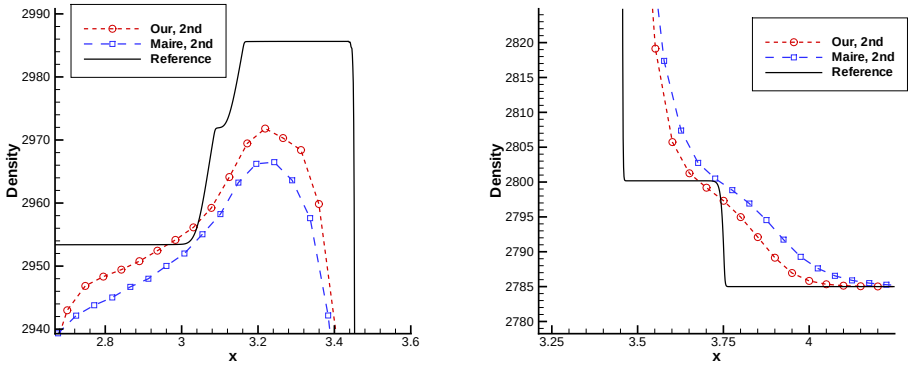


Figure 11: Wilkins' problem. Local comparison between the computed densities by the current 2nd-order scheme and those by Maire et al.'s 2nd-order scheme with 100 cells around the elastic rarefaction and shock waves.

5.4 Collapse of a cylindrical beryllium shell

This problem initially proposed by Howell and Ball in [17] is to compute the collapse of a cylindrical beryllium shell. The problem setting is depicted in Fig. 12.

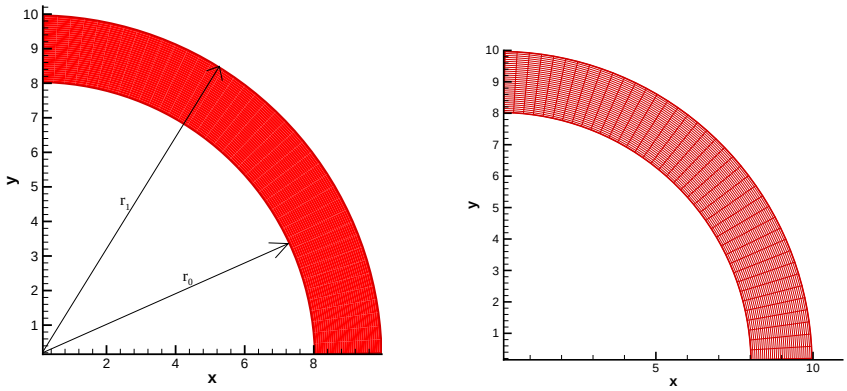


Figure 12: Collapse problem: Sketch map (left) and the initial gird (right).

The initial inner and outer radii of the shell are $R_i = 0.08\ m$ and $R_o = 0.10\ m$, respectively. The angle range of computational field is $[0, \frac{\pi}{2}]$. The initial density $\rho_0 = 1845\ kg/m^3$, the initial pressure $p_0 = 10^5\ Pa$, the initial velocity is towards the center of the shell and the initial radial velocity field is $-V_0 \frac{R_i}{r}$, where V_0 is 417.1 m/s and $r = \sqrt{x^2+y^2}$ is the radius. The equation of state for beryllium is given by the Mie-Grüneisen model with the following parameters: $\rho_0 = 1845\ kg/m^3$, $a_0 = 12870\ m/s$, $\Gamma_0 = 2$,$s = 1.124$. The constitutive model is characterized by the following parameters: the shear module $\mu = 151.9 \times 10^9\ Pa$, the yielding strength $Y^0 = 330 \times 10^6\ Pa$. In this problem, on the left and right boundaries

https://doi.org/10.4208/cicp.OA-2016-0173 Published online by Cambridge University Press

the reflected boundary condition is imposed, and on the upper and down boundaries the free boundary condition is implemented.

For this problem, Maire et al. in [4] pointed out that the analytic solution proposed by Howell and Ball in [17] is also suitable for this problem with a different EOS. The analytic solution is that, at time t=130 μs, the initial total kinetic energy is totally transformed into the internal energy and the inner and outer stopping radii become 0.05 m and 0.0781 m, respectively.

We use two grids (20×16 and 40×32) to simulate the problem in order to analyze the convergence of the current second-order scheme. In Fig. 13 one can see that the inner and outer stopping radii of the shell agree with the theoretical values and the numerical solution is converging to the analytical one. This shows that the current scheme appears to be convergent.

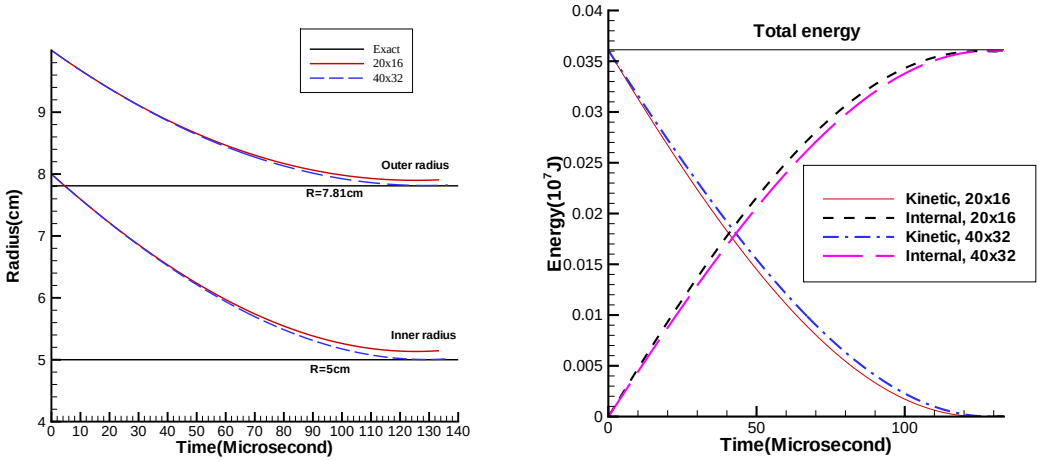


Figure 13: Collapse problem: Average radius and the energy vs time with different cells.

From Fig. 14, one can observe that the changes of the inner and outer radii of the shell with the time at different angles are almost the same. This demonstrates that the current second-order scheme seems to be symmetrical. We further see that the density contours seem to be symmetrical, and the minimum and maximum of the density computed by the current scheme are 1842.04 kg/m^3 and 1843.74 kg/m^3 respectively. However, the minimum and maximum of the computed density by Maire et al.'s scheme in [4] are 1843.8 kg/m^3 and 1844.8 kg/m^3 respectively.

Obviously, in our numerical results, the minimum and maximum values of the density are slightly smaller than the corresponding computed values of the density evaluated by Maire et al. in [4]. The reason, we think, is that during evaluating rarefaction waves the numerical dissipation of the our 2nd-order scheme is less than that of Maire et al.'s 2nd-order scheme. For this collapse problem, the rarefaction waves dominate in the flow and FRRSE is constructed based on rarefaction waves, thus resulting in less numerical

https://doi.org/10.4208/cicp.OA-2016-0173 Published online by Cambridge University Press

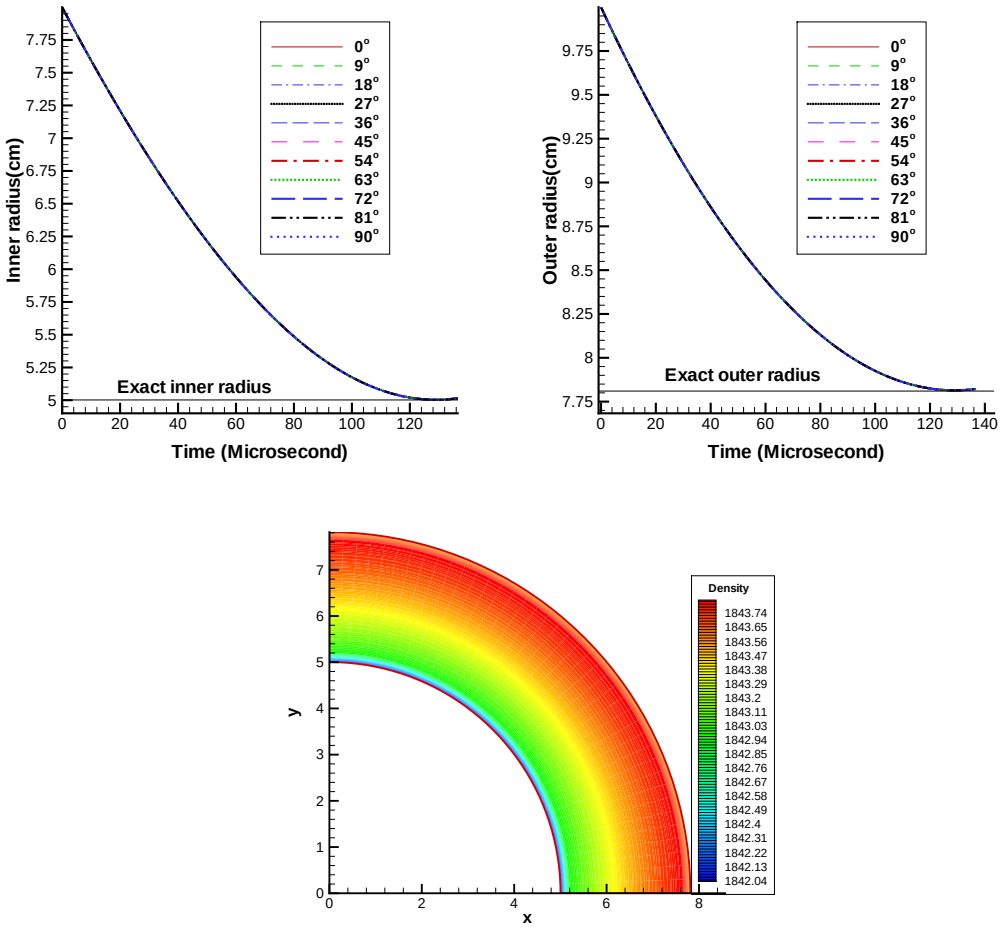


Figure 14: Collapse problem: Inner radius (left) and outer radius (center) versus time at different angles with 40×32 cells and the density contours (right) at time $t=130$ μs with 40×32 cells.

dissipation. Less numerical dissipation makes deformation of the beryllium shell easy and hence the change of the density in our numerical results is greater than that in [4].

5.5 Two-dimensional projectile impact

Here we consider a 2D impact problem, in which an aluminium is projected against a rigid wall. We use the same data as those in [4]. The initial projectile is a rectangular plate and its length and thickness are 5 m and 1 m respectively. The material is made of aluminium, for which the equation of state is given by the Mie-Grüneisen model with parameters: $\rho_0=2785$ kg/m^3, $a_0=5328$ m/s, $\Gamma_0=2$,$s=1.338$. The constitutive model is characterized by the following parameters: the shear module $\mu=27.6\times10^9$ Pa, the

https://doi.org/10.4208/cicp.OA-2016-0173 Published online by Cambridge University Press

Table 3: Length of the projectile for two grids.

Grid	Stopping time($10^{-6}s$)	Length(cm)
50×10	4511.2	464.0
100×20	4844.9	461.4

yielding strength $Y^0 = 300\times10^6\ Pa$. We take the initial computational domain to be $[0{,}5\ m]\times[0{,}1\ m]$ and the initial velocity to be $(-150\ m/s, 0\ m/s)$. Besides, on the left boundary the reflected boundary condition is imposed, while on other three boundaries, the free boundary condition is implemented.

Although this problem has neither analytical solution nor experimental results, it is a good example to test the robustness and accuracy of our numerical scheme. In order to perform a convergence analysis, we use two initial uniformly spaced grids 50×10 and 100×20 to simulate this problem.

When it impacts the wall, the projectile deforms and its kinetic energy is transformed to the internal energy. When all kinetic energy is completely transformed into the internal energy, the projectile begins to rebound. We define the stopping time by the moment when 99.99% of the kinetic energy is transformed into the internal energy.

We present the stopping time and the length of the projectile in Table 3, From which one sees that, when the grid is refined, the stopping time is longer and the length of the projectile is shorter. This shows the current scheme is convergent. The grid is refiner, the numerical dissipation is smaller. This results in slowdown of transform of the kinetic energy into the internal energy, and so the stopping time computed by using the refined grid is longer and the length is shorter. Besides, we find that the our computed final length is close to the value given by Maire et al.'s second-order scheme. The computed final length computed by the current scheme with 100×20 cells is 461.4 cm, but the final length computed by Maire et al.'s second scheme with 100×20 and 200×40 cells are about 464.0 cm and 462.0 cm, respectively. This shows that the current scheme is less numerically dissipative than Maire et al.'s second-order scheme in same number of cells.

The changes of length and energy with respect to time are given in Fig. 15 from which one can see that the transform of the kinetic energy into the internal energy with a coarse grid is faster than that with a refined grid. This is consistent with the analysis mentioned above. Moreover, we find that after the stopping time, the length of the projectile starts to become big, and this shows that the projectile begins to rebound.

At last, let us see that the final grid and density contours in Figs. 16 and 17, from which we see that the evaluated final grid and density contours are symmetrical with respect to the line $y = 0.5\ m$. This illustrates that our scheme appears to be symmetrical. Otherwise, one can observe that there are very clear wave structures in these figures. Moreover, the refiner the grid is, the clearer the wave structures are; but the positions of waves are almost the same. Such wave structures can not be found in [4].

https://doi.org/10.4208/cicp.OA-2016-0173 Published online by Cambridge University Press

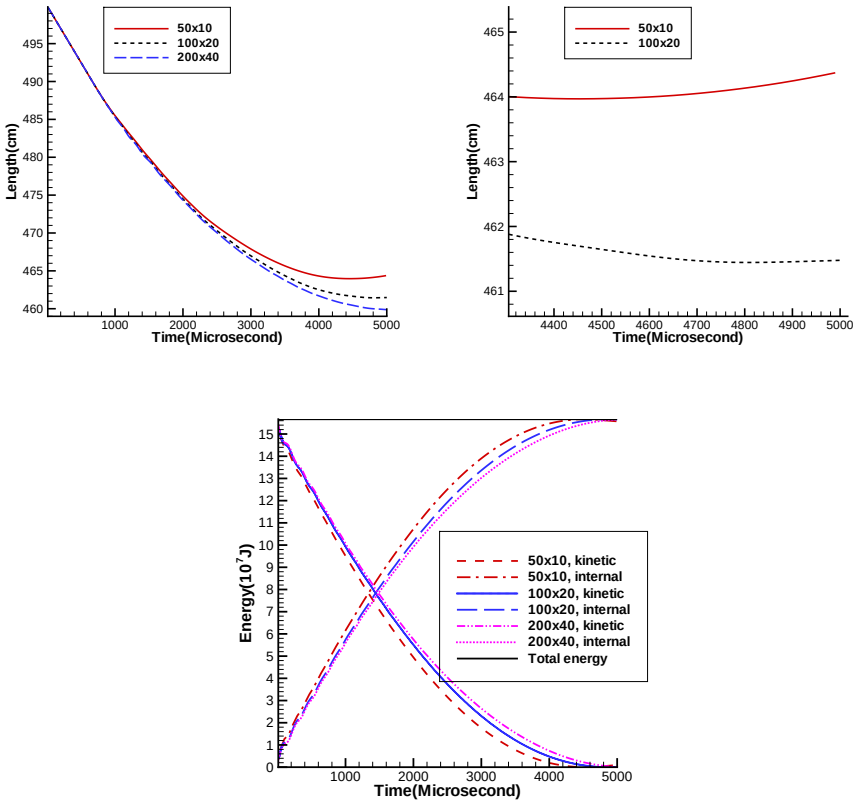


Figure 15: Projectile problem: length vs time with different cells.

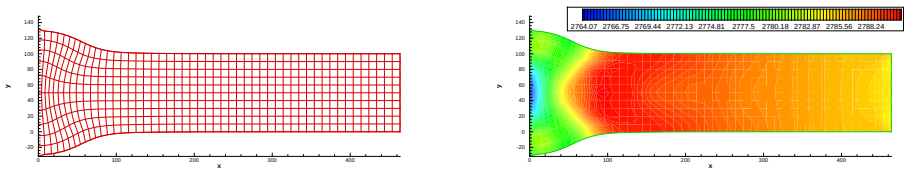


Figure 16: Two-dimensional projectile impact problem: Final grid (top) and the density contours (bottom) at the stopping time $t=4.5\times10^{-3}$ s with 50×10 cells.

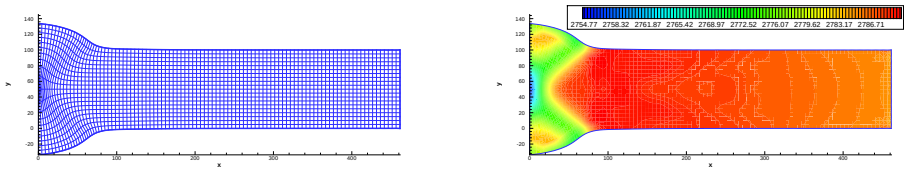


Figure 17: Two-dimensional projectile impact problem: Final grid (top) and density contours (bottom) at the stopping time $t=4.9\times10^{-3}$ s with 100×20 cells.

https://doi.org/10.4208/cicp.OA-2016-0173 Published online by Cambridge University Press

6 Conclusions

In this paper we have introduced a four-rarefaction approximate Riemann solver for the equations of two-dimensional elastic-plastic flows with the Mie-Grüneisen equation of state and Wilkins's constitutive model, where the von Mises' yielding condition is used. Then, based on the developed Riemann solver, we have proposed a predictor-corrector finite volume scheme to discretize in time and a WENO reconstruction to discretize in space for the two-dimensional equations for elastic-plastic flows in the Lagrangian framework, in which the discretization in both space and time is of second-order accuracy. At cell interfaces, the constructed four-rarefaction Riemann solver is used to evaluate the Godunov state for the density, pressure, velocity and stress. In summary, we have constructed a second-order cell-centered Lagrangian scheme, which has been tested numerically through a number of test problems, including the piston problem and Wilkins' problem. The numerical results have demonstrated that the computed solutions with the present scheme appear to converge to the exact solution and show good agreement with other reference solutions. Moreover, compared with the numerical results reported by Maire and collaborators, it can be seen that the present scheme exhibits comparable accuracy for shock waves, while being more accurate in simulating rarefaction waves. Finally, it is worth remarking that the current scheme has the potential to be extended to very high order of accuracy in both space and time.

Acknowledgments

This work was supported by the Science and Technology Foundation of CAEP (Grant No. 2013A0202011), the National Basic Research Program under Grants (2014CB745002, 2014CB239202, 2011CB309705), NSFC (Grant Nos. 11172050, 11672047, 11229101, 11371065 and 11271051), Science Challenge Project (Grant No. TZ2016002) and Shandong Province Natural Science Foundation of China (No. ZR2011EL035).

A Evaluating the states behind a TSW

For a TSW, we choose s_{xy} as an independent variable and other variables as the dependent variables. Given the state ahead of a TSW, $\mathbf{W}_a$ and $s_{xy,b}$, we need to evaluate other dependent variables, such as ρ_b, u_b, v_b, p_b, $s_{xx,b}$ and $s_{yy,b}$.

If the deviatoric stresses reach the elastic limit, the states do not change again for a TSW. Here we assume, during evaluating a TSW, the deviatoric stresses do not reach the elastic limit. We shall discuss the elastic limit for a TSW in Appendix B.

Integrating (3.18)-(3.19) with respect to τ from τ_a to τ_b where $\tau=\frac{1}{2}s_{xy}^2$, one has

$$\mathbf{T}_b=\mathbf{T}_a+\int_{\tau_a}^{\tau_b}\mathbf{H}d\tau,\quad \mathbf{T}=[\rho,p,s_{xx},s_{yy}]^T,\quad \mathbf{H}=\left[H_\rho,H_p,H_{xx},H_{yy}\right]^T, \tag{A.1}$$

https://doi.org/10.4208/cicp.OA-2016-0173 Published online by Cambridge University Press

where $H_p=\frac{(w_3-\frac{4\mu}{3\rho}w_2)}{\rho s_1^2}$, $H_\rho=\frac{w_2}{\rho s_1^2}$, $H_{xx}=\frac{(1+\frac{2\mu}{3\rho}w_2)}{\rho s_1^2}$, $H_{yy}=-\frac{(1+\frac{4\mu}{3\rho}w_2)}{\rho s_1^2}$.

Next, we consider how to approximate the integral term in (A.1):

$$\xi(\tau_b)=\int_{\tau_a}^{\tau_b}\mathbf{H}d\tau \tag{A.2}$$

with high-order accuracy, where $\xi(\tau_b)=\left(\xi_\rho(\tau_b),\xi_p(\tau_b),\xi_{s_{xx}}(\tau_b),\xi_{s_{yy}}(\tau_b)\right)^T$.

Obviously, we can not get an explicit formulation of $\xi(\tau_b)$. Thus, we use the Gaussian quadrature method to compute $\xi(\tau_b)$ with high-order accuracy:

$$\widehat{\xi}_b=\sum_{g=1}^{G}\omega_g\mathbf{H}(\tau_g)(\tau_b-\tau_a), \tag{A.3}$$

where τ_g and ω_g are the Gaussian quadrature points and integral weights respectively, G is the number of the Gaussian quadrature points.

From (3.6) and (3.9), we find that, given $\mathbf{T}(\tau_g)$ and $s_{xy,g}$, we can evaluate the value of $\mathbf{H}(\tau_g)$. In the following, we describe how to evaluate $\mathbf{T}(\tau_g)$ with given $\mathbf{T}(\tau_{g-1})$. (3.18)-(3.19) can be written as $d\mathbf{T}=\mathbf{H}d\tau$. Integrating this equation from τ_{g-1} to τ_g yields

$$\mathbf{T}(\tau_g)=\mathbf{T}(\tau_{g-1})+\int_{\tau_{g-1}}^{\tau_g}\mathbf{H}d\tau. \tag{A.4}$$

Assume that both left and right TSWs are rarefaction waves, $\mathbf{H}$ is smooth. We make a Taylor series expression at τ_{g-1} for $\mathbf{H}$:

$$\mathbf{H}(\tau)=\mathbf{H}_{g-1}+\sum_{m=1}^{M}\frac{\partial^m\mathbf{H}}{\partial\tau^m}\frac{(\tau-\tau_{g-1})^m}{m!}. \tag{A.5}$$

Substituting (A.5) into (A.4), we see that

$$\mathbf{T}_g=\mathbf{T}_{g-1}+\mathbf{H}_{g-1}(\tau_g-\tau_{g-1})+\sum_{m=1}^{M}\frac{\partial^m\mathbf{H}}{\partial\tau^m}\frac{(\tau_g-\tau_{g-1})^{m+1}}{(m+1)!}. \tag{A.6}$$

Given $\mathbf{T}_g$, one evaluates a_g^2, $s_{1,g}^2$, $s_{2,g}^2$, $H_{\rho,g}$, $H_{p,g}$, $H_{xx,g}$ and $H_{yy,g}$ and correspondingly one can get the values of $\widehat{\ }_b$ in (A.3).

Integrating (3.20) with respect to τ from τ_a to τ_b, one infers that

$$v_b=v_a\mp\int_{\tau_a}^{\tau_b}\frac{1}{\rho^2 s_1}w_2d\tau. \tag{A.7}$$

With the help of the given values of $\mathbf{T}_g$, a_g^2, $s_{1,g}^2$, $s_{2,g}^2$ and $H_{\rho,g}$ $(g=1,\cdots,G)$, we can employ the Gaussian quadrature method to compute v_b:

$$v_b=v_a\mp\sum_{g=1}^{G}\omega_g\frac{H_{\rho,g}s_{1,g}}{\rho_g}(\tau_b-\tau_a). \tag{A.8}$$

https://doi.org/10.4208/cicp.OA-2016-0173 Published online by Cambridge University Press

If one integrates (3.20) with respect to s_{xy} from $s_{xy,a}$ to $s_{xy,b}$, one obtains

$$u_b = u_a \pm \int_{s_{xy,a}}^{s_{xy,b}} \frac{1}{\rho s_1} ds_{xy}. \tag{A.9}$$

Given the values of $\mathbf{T}_g$, $s_{1,g}^2$ and $s_{2,g}^2$ ($g=1,\cdots,G$), we can use the Gaussian quadrature method to compute u_b:

$$u_b = u_a \pm \sum_{g=1}^{G} \omega_g \frac{1}{\rho_g s_{1,g}} (s_{xy,b} - s_{xy,a}). \tag{A.10}$$

Remark A.1. From the numerical experiments we find: if $G = \max\{2, 16 \times \frac{|s_{xy,b}|-|s_{xy,a}|}{|s_{xy,b}|+|s_{xy,a}|}\}$ in (A.3) and $M=1$ in (A.5), the approximations in (A.6), (A.8) and (A.10) are high-order accurate.

B Evaluation of the stress yielding limit across a TSW

Given the state, $\mathbf{W}_a$, ahead of a TSW, we need to decide the states of the stress yielding limit behind the TSW. These unknown yielding limit states are named $\mathbf{W}_b^E$, where $\mathbf{W}_b^E = \left(\rho_b^E, u_b^E, v_b^E, p_b^E, s_{xx,b}^E, s_{yy,b}^E, s_{xy,b}^E\right)^T$. In the following, we show how to evaluate the yielding limit states for a TSW. Here, $s_{xy,b}^E$ is the independent variable and other variables are dependent. Define

$$\vartheta(\tau^E) = \sqrt{\mathbf{S}^E : \mathbf{S}^E} - \sqrt{\frac{2}{3}} Y^0, \tag{B.1}$$

where $\tau^E = \frac{1}{2}(s_{xy,b}^E)^2$, $\mathbf{S}^E$ is the yielding limit of stresses. By virtue of von Mises' yielding condition, $\vartheta(\tau^E) = 0$. Obviously, we still can not give an explicit solution and have to use the Newton iteration method to solve it. In the following, we describe the detailed procedure of the iteration.

Step 1: Define the first iteration values: $s_{xy}^{(1)} = s_{xy,a}$, $s_{xx}^{(1)} = s_{xx,a}$, $s_{yy}^{(1)} = s_{yy,a}$, $p^{(1)} = p_a$, $\rho^{(1)} = \rho_a$ and $\tau^{(1)} = \frac{1}{2} s_{xy,a}^2$.

Step 2: Evaluate $\vartheta(\tau^{(k)}) = \sqrt{\mathbf{S}^{E,(k)} : \mathbf{S}^{E,(k)}} - \sqrt{\frac{2}{3}} Y^0$. If $|\vartheta(\tau^{(k)})| < 10^{-16}$, then iteration procedure is stopped, and set $s_{xy,b}^E = s_{xy}^{(k)}$, $s_{xx,b}^E = s_{xx}^{(k)}$, $s_{yy,b}^E = s_{yy}^{(k)}$, $p_b^E = p^{(k)}$, $\rho_b^E = \rho^{(k)}$, $u_b^E = u^{(k)}$, $v_b^E = v^{(k)}$.

Step 3: Evaluate the derivative of $\vartheta(\tau^{(k)})$ with respect to $\tau^{(k)}$:

$$\frac{d\vartheta(\tau^{(k)})}{d\tau^{(k)}} = \frac{\partial \vartheta(s_{xy,b}^E)^{(k)}}{\partial \tau^{(k)}} + \frac{\partial \vartheta(\tau^{(k)})}{\partial s_{xx}^{(k)}} \frac{ds_{xx}^{(k)}}{d\tau^{(k)}} + \frac{\partial \vartheta(\tau^{(k)})}{\partial s_{yy}^{(k)}} \frac{ds_{yy}^{(k)}}{d\tau^{(k)}}, \tag{B.2}$$

https://doi.org/10.4208/cicp.OA-2016-0173 Published online by Cambridge University Press

where $\frac{ds_{xx}^{(k)}}{d\tau^{(k)}}$ and $\frac{ds_{yy}^{(k)}}{d\tau^{(k)}}$ can be computed by using (3.19) respectively, and the detailed procedure will be omitted here.

Step 4: Evaluate the next iteration value of τ and s_{xy}:

$$\tau^{(k+1)}=\tau^{(k)}-\frac{\vartheta(\tau^{(k)})}{\frac{d\vartheta(\tau^E)^{(k)}}{d\tau^{(k)}}},\qquad s_{xy,b}^{(k+1)}=\sqrt{2\tau^{(k+1)}}\,\mathrm{sign}\left(1,s_{xy,b,old}\right),$$

where $s_{xy,b,old}$ is the solution to the problem of two TSWs without using von Mises' yielding condition.

Step 5: Use the method introduced in the above subsection to evaluate the values of $s_{xx}^{(k+1)}$, $s_{yy}^{(k+1)}$, $p^{(k+1)}$, $\rho^{(k+1)}$, $u^{(k+1)}$ and $v^{(k+1)}$ across the TSW.

Step 6: Convergence decision. Stop the iteration procedure whenever CHA $=\frac{\left|\tau^{(k+1)}-\tau^{(k)}\right|}{\frac{1}{2}\left|\tau^{(k+1)}+\tau^{(k)}\right|}<10^{-16}$. Otherwise, go to Step 2 with $k:=k+1$.

C Evaluating the states behind a LSW

For a LSW, we choose the density ρ as the independent variable and other variables as the dependent ones. Integrating (3.21) across the left or right LSW, one gets

$$u_b=u_a,\quad v_b=v_a\mp\int_{\rho_a}^{\rho_b}\frac{s_2}{\rho}d\rho,\quad p_b=p_a+\int_{\rho_a}^{\rho_b}\left(s_2^2-\frac{4\mu}{3\rho}\right)d\rho, \tag{C.1}$$

$$s_{xx,b}=s_{xx,a}+\int_{\rho_a}^{\rho_b}\frac{2\mu}{3\rho}d\rho=s_{xx,a}+\frac{2\mu}{3}\left[\ln(\rho_b)-\ln(\rho_a)\right], \tag{C.2}$$

$$s_{yy,b}=s_{yy,a}+\int_{\rho_a}^{\rho_b}-\frac{4\mu}{3\rho}d\rho=s_{yy,a}-\frac{4\mu}{3}\left[\ln(\rho_b)-\ln(\rho_a)\right], \tag{C.3}$$

$$s_{xy,b}=s_{xy,a},\quad \sqrt{\frac{3}{2}\mathbf{S}_b:\mathbf{S}_b}\le Y^0. \tag{C.4}$$

In (C.1), $-$ and $+$ stand for the left and right LSWs, respectively.

Substituting (3.6) into (C.1) results in

$$p_b=p_a+\int_{\rho_a}^{\rho_b}\left(a^2-\frac{\rho_0}{\rho^2}\Gamma_0 s_{yy}\right)d\rho=p_a+\chi(\rho_b), \tag{C.5}$$

where $\chi(\rho_b)=\int_{\rho_a}^{\rho_b}\left(a^2-\frac{\rho_0}{\rho^2}\Gamma_0 s_{yy}\right)d\rho$.

Still, we can not give an explicit expression of the integral $\chi(\rho_b)$ in (C.5) and shall use the Gaussian quadrature method to evaluate it: $\widehat{\chi}_b=(\rho_b-\rho_a)\sum_{g=1}^{G_L}\omega_g a^2(\rho_g)-\rho_0\Gamma_0(\rho_b-\rho_a)\sum_{g=1}^{G_L}\omega_g\frac{s_{yy}(\rho_g)}{\rho_g^2}$.

In the following, we give the detailed procedure of evaluating $\widehat{\chi}_b$.

https://doi.org/10.4208/cicp.OA-2016-0173 Published online by Cambridge University Press

Step 1: evaluate $s_{yy}(\rho_g)$ and update $\mathbf{S}_g$.

We integrate (3.21) from ρ_a to ρ_g to obtain

$$s_{xx,g}=s_{xx,a}+\frac{2\mu}{3}\left[\ln(\rho_g)-\ln(\rho_a)\right],\quad s_{yy,g}=s_{yy,a}-\frac{4\mu}{3}\left[\ln(\rho_g)-\ln(\rho_a)\right],$$

where $s_{xx,g}=s_{xx}(\rho_g)$, $s_{xy,g}=s_{xy}(\rho_g)$ and $s_{yy,g}=s_{yy}(\rho_g)$.

Then the condition of von-Mises' elastic limit is used to update $\mathbf{S}_g$.

Step 2: evaluate $a^2(\rho_g)$.

From (3.4), one sees that, given ρ_g and $p(\rho_g)$, one can evaluate the value of $a^2(\rho_g)$. Next, we show how to evaluate $p(\rho_g)$ with given $p(\rho_{g-1})$.

An integration of (3.21) from ρ_{g-1} to ρ_g gives

$$p(\rho_g)=p_{g-1}+\int_{\rho_{g-1}}^{\rho_g}\left(a^2-\frac{\rho_0}{\rho^2}\Gamma_0 s_{yy}\right)d\rho. \tag{C.6}$$

Here the integral term can be written as

$$\int_{\rho_{g-1}}^{\rho_g}\left(a^2-\frac{s_{yy}}{\rho^2}\rho_0\Gamma_0\right)d\rho=\phi-\rho_0\Gamma_0\sum_{g_i=1}^{2}\omega_{g_i}\frac{s_{yy}(\rho_{g_i})}{(\rho_{g_i})^2}(\rho_g-\rho_{g-1}), \tag{C.7}$$

where ω_{g_i} and ρ_{g_i} are the weights and density values at the g_i-th Gaussian quadrature point between ρ_{g-1} and ρ_g respectively, and

$$\phi=\int_{\rho_{g-1}}^{\rho_g}a^2 d\rho. \tag{C.8}$$

We shall approximate (C.8) with high-order accuracy. Assume that both left and right waves are rarefaction waves and a^2 is smooth. We make a Taylor series expansion at ρ_{g-1} for a^2:

$$a^2(\rho)=a^2_{g-1}+\sum_{m=1}^{M_L}\frac{\partial^m a^2}{\partial\rho^m}\frac{(\rho-\rho_{g-1})^m}{m!}. \tag{C.9}$$

Inserting (C.9) into (C.8), we find that

$$\phi=a^2_{g-1}(\rho_g-\rho_{g-1})+\sum_{m=1}^{M_L}\frac{\partial^m a^2}{\partial\rho^m}\frac{(\rho_g-\rho_{g-1})^{m+1}}{(m+1)!}. \tag{C.10}$$

Thanks to (C.6), (C.7) and (C.10), one obtains the approximation to $p(\rho_g)$:

$$p_g=p_{g-1}+a^2_{g-1}\triangle\rho_g+\sum_{m=1}^{M_L}\frac{\partial^m a^2}{\partial\rho^m}\frac{(\triangle\rho_g)^{m+1}}{(m+1)!}-\rho_0\Gamma_0\sum_{g_i=1}^{2}\omega_{g_i}\frac{s_{yy}(\rho_{g_i})}{(\rho_{g_i})^2}(\triangle\rho_g). \tag{C.11}$$

https://doi.org/10.4208/cicp.OA-2016-0173 Published online by Cambridge University Press

Given the values of p_g, one can use (3.4) to evaluate a_g^2 ($g=1,\cdots,G_L$), where a_g^2 is the approximation to $a^2(\rho_g)$.

Finally, the approximation to $\widehat{\chi}_b$ reads as

$$\chi_b=(\rho_b-\rho_a)\sum_{g=1}^{G_L}\omega_g a_g^2-\rho_0\Gamma_0(\rho_b-\rho_a)\sum_{g=1}^{G_L}\omega_g\frac{s_{yy}(\rho_g)}{\rho_g^2}, \tag{C.12}$$

and the approximation to p_b in (C.5) can be obtained. We refer the reader to [14] on the error analysis for this approximation. We do not want to repeat the details here.

As before, we use the Gaussian quadrature method to evaluate v_b:

$$v_b=v_a\mp\sum_{g=1}^{G_L}\omega_g\frac{s_2(\rho_g)}{\rho_g}(\rho_b-\rho_a), \tag{C.13}$$

where $s_2(\rho_g)$ is approximated by (3.6) with given ρ_g, p_g and $\mathbf{S}_g$ ($g=1,\cdots,G_L$).

In the numerical experiments, we find that $G_L=\max\{2,16\times\frac{|\rho_b-\rho_a|}{|\rho_b+\rho_a|}\}$ in (C.12) and (C.13), and $M_L=2$ in (C.11) is good enough to obtain the desired high-order accuracy.

D Solving the problem of two TSWs in (3.28)

In this subsection, we show how to solve (3.28) with given initial states in front of the left and right TSWs.

Define $\Lambda(s_{xy}^{T*})=u_L^{T*}(s_{xy}^{T*})-u_R^{T*}(s_{xy}^{T*})$,where $s_{xy}^{T*}=s_{xy,L}^{T*}=s_{xy,R}^{T*}$. According to (3.28), $\Lambda(s_{xy}^{T*})=u_L^{T*}(s_{xy}^{T*})-u_R^{T*}(s_{xy}^{T*})=0$.

As before, we employ the Newton iteration method to solve it as follows.

Step 1: Guess the initial $s_{xy(1)}^{T*}$ as $s_{xy,(k)}^{T*}=\frac{1}{2}\left(s_{xy,L}+s_{xy,R}\right)$, where $k=1$.

Step 2: Given the value of $s_{xy,(k)}^{T*}$, without using von Mises' yielding condition, one can evaluate the states behind two TSWs ($u_{m,(k)}^{T*}$, $v_{m,(k)}^{T*}$, $\rho_{m,(k)}^{T*}$, $p_{m,(k)}^{T*}$, $s_{xx,m,(k)}^{T*}$, $s_{yy,m,(k)}^{T*}$, $m=L,R$). Denote $\Lambda_{(k)}$ by $\Lambda_{(k)}=u_{L,(k)}^{T*}-u_{R,(k)}^{T*}$.

Step 3: Evaluate the derivatives of $\Lambda_{(k)}$ with respect to $s_{xy,(k)}^{T*}$:

$$\frac{d\Lambda_{(k)}}{ds_{xy,(k)}^{T*}}=\frac{du_{L,(k)}^{T*}}{ds_{xy,(k)}^{T*}}-\frac{du_{R,(k)}^{T*}}{ds_{xy,(k)}^{T*}}=\frac{1}{\rho_{L,(k)}^{T*}s_{1,L,(k)}^{T*}}+\frac{1}{\rho_{R,(k)}^{T*}s_{1,R,(k)}^{T*}}.$$

Step 4: Evaluate $s_{xy,(k+1)}^{T*}=s_{xy,(k)}^{T*}-\frac{\Lambda_{(k)}}{\frac{d\Lambda_{(k)}}{ds_{xy,(k)}^{T*}}}$.

Step 5: Evaluate the errors of the iteration:

$$\mathrm{CHA}=\max\left\{\left|s_{xy,(k+1)}^{T*}-s_{xy,(k)}^{T*}\right|,\Lambda_{(k)}\right\}.$$

https://doi.org/10.4208/cicp.OA-2016-0173 Published online by Cambridge University Press

Go to **Step 6** if CHA $<10^{-8}$; otherwise, go to **Step 2** with $K:=K+1$.

Step 6: Check whether the states behind two TSWs reach the elastic limit. Because the left and right states may reach the elastic limit, there are four cases we have to consider:

If $\sqrt{\frac{3}{2}S_L^{T*}:S_L^{T*}}<Y^0$ and $\sqrt{\frac{3}{2}S_R^{T*}:S_R^{T*}}<Y^0$, the evaluation of (3.28) stops;

If $\sqrt{\frac{3}{2}S_L^{T*}:S_L^{T*}}<Y^0$ and $\sqrt{\frac{3}{2}S_R^{T*}:S_R^{T*}}\geq Y^0$, go to Step 7A;

If $\sqrt{\frac{3}{2}S_L^{T*}:S_L^{T*}}\geq Y^0$ and $\sqrt{\frac{3}{2}S_R^{T*}:S_R^{T*}}<Y^0$, go to Step 7B;

If $\sqrt{\frac{3}{2}S_L^{T*}:S_L^{T*}}\geq Y^0$ and $\sqrt{\frac{3}{2}S_R^{T*}:S_R^{T*}}\geq Y^0$, go to Step 7C.

Step 7A: Left torsional solution.

In this case, $W_R^{T*}=W_R^E$, where W_R^E is the elastic limit state behind the right TSW and determined by using the method introduced in Appendix B.

Because the deviatoric stress of the left states does not reach the elastic limit, one can change $s_{xy,L}^{T*}$ to make $u_L^{T*}=u_R^{T*}$, but s_{xy} may not be continuous across the linear degenerate wave. Now, we need to solve the following equation to obtain the left state:

$$u_L^{T*}(s_{xy,L}^{T*})=u_R^{T*}.$$

We solve this equation still by using the Newton iteration without considering the elastic limit. Here we do not show the details for the simplicity of presentation.

After the convergence of iteration, if $\sqrt{\frac{3}{2}S_L^{T*}:S_L^{T*}}<Y^0$, Step 7A is finished. If $\sqrt{\frac{3}{2}S_L^{T*}:S_L^{T*}}\geq Y^0$, the state behind the left TSW reaches the elastic limit. Consequently, $W_L^{T*}=W_L^E$, where W_L^E is the elastic limit state behind the left TSW. So far, the evaluation of (3.28) is complete.

Step 7B: Right torsional solution.

In this case, $W_L^{T*}=W_L^E$. we need to solve the following equation to obtain the right state: $u_R^{T*}(s_{xy,R}^{T*})=u_L^{T*}$ We solve this problem by using the Newton iteration without considering the elastic limit. Here we do not show the details for simple presentation.

After the iteration has converged, Step 7B is ended if $\sqrt{\frac{3}{2}S_R^{T*}:S_R^{T*}}<Y^0$, or else $W_R^{T*}=W_R^E$. Now, the evaluation of (3.28) is complete.

Step 7C: Two elastic limits.

Because the stresses of the left and right states reach the elastic limit, $W_L^{T*}=W_L^E$ and $W_R^{T*}=W_R^E$. Now, (3.28) is solved.

References

[1] M.L.Wilkins, Methods in computational physics, Volume 3, Chapter Calculation of elastic-plastic flow, Academic press, 1964, pp.211-263.

[2] D.E. Burton, T.C. Carney, N.R. Morgan, S.K. Sambasivan, M.J. and Shashkov, A cell-centered Lagrangian Godunov-like method for solid dynamics, Comput. Fluids, 83(2013), 33-47; http://dx.doi.org/10.1016/j.compfluid. 2012.09.08.

https://doi.org/10.4208/cicp.OA-2016-0173 Published online by Cambridge University Press

[3] G. Kluth, B. Després, Discretization of hyperelasticity on unstructured mesh with a cell-centered Lagrangian scheme, J. Comput. Physics., 229(2010), 9092-9118.
[4] P.-H. Maire, R. Abgrall, J. Breil, R. Loubère, B. Rebourcet, A nominally second-order cell-centered Lagrangian scheme for simulating elastic-plastic flows on two-dimensional unstructured grids, J. Comput. Physics., 235(2013), 626-665.
[5] S. K. Sambasivan, R. Loubère and M.J. Shashkov, a finite volume lagrangian cell-centered mimetic approach for computing elasto-plastic deformation of solids in general unstructed grids, 6th European Congress on Computational Methods in Applied Sciences and Engineering 2012 (ECCOMAS 2012), Vienna, Austria, 10 September 2012 through 14 September 201.
[6] B. Després. A geometrical approach to non-conservative shocks and elastoplastic shocks. Arch. Rational Mech. Anal., 186(2)(2007), 175-308.
[7] S.L. Gavrilyuk, N. Favrie and R. Saurel. Modeling wave dynamics of compressible elastic materials. J. Comput. Physics., 227(2008), 2941-2969.
[8] D.J. Hill, D. Pullin, M. Ortiz and D. Meiron. An Eulerian hybrid WENO centered-difference solver for elastic-plastic solids. J. Comput. Physics., 229(2010), 9503-9072.
[9] G.H. Miller and P. Collela. A high-order Eulerian Godunov method for elastic-plastic flow in solids, J. Comput. Physics., 167(2001), 131-176.
[10] J.A. Trangenstein and P. Collela. A high-order Godunov method for modeling finite deformation in elastic-plastic solids, Communications on Pure and Applied mathematics, XLIV, 1991, 41-100.
[11] P.T. Barton, D. Drikakis, E. Romenski and V.A. Titarev. Exact and approximate solutions of Riemann problems in non-linear elasticity, J. Comput. Physics., 228(2009), 7046-7068.
[12] V.A. Titarev, E. Romenski and E. F. Toro. MUSTA-type upwind fluxes for non-linear elasticity, International Journal for Numerical Methods in Engineering., 73(2008), 897-926.
[13] David Kahaner, Cleve Moler, Stephen Nash. Numerical methods and software. Prentice-Hall, ISBN 978-0-13-627258-8, 1989.
[14] Jun-bo Cheng, Eleuterio F. Toro, Song Jiang, Ming Yu, and Weijun Tang. A high-order cell-centered Lagrangian scheme for one-dimensional elastic-plastic problems. Computer and Fluids, 122(2015), 136-152, Doi: 10.1016/j.compfluid.2015.08.029, 2015.
[15] P. J. Roache. Code verification by the method of manufactured solutions. Trans. ASME, J. Fluids Engineering, 124(2002), 4-10.
[16] K. Salari and P. Knupp. Code verification by the method of manufactured solutions. Sandia Report, Sandia National Laboratories, SAND2000-1444, 2000.
[17] B.P. Howell and G.J. Ball. A free-Lagrange augmented Godunov method for the simulation of elastic-plastic solids. J. Comput. Phys., 175(2002), 128-167.
[18] E F Toro. Riemann solvers and numerical methods for fluid dynamics, Springer, 3rd edition, 2009.

https://doi.org/10.4208/cicp.OA-2016-0173 Published online by Cambridge University Press